Sources of organic aerosols in eastern China: A modeling study with high-resolution intermediate-volatility and semi-volatile organic compound emissions

Jingyu An[1], Cheng Huang[1*], Dandan Huang[1], Momei Qin[2,1], Huan Liu[3], Rusha Yan[1], Liping Qiao[1], Min Zhou[1], Yingjie Li[1], Shuhui Zhu[1], Qian Wang[1], Hongli Wang[1]

1. State Environmental Protection Key Laboratory of the Formation and Prevention of Urban Air Pollution Complex, Shanghai Academy of Environmental Sciences, Shanghai 200233, China

2. Jiangsu Key Laboratory of Atmospheric Environment Monitoring and Pollution Control, Collaborative Innovation Center of Atmospheric Environment and Equipment Technology, Nanjing University of Information Science & Technology, Nanjing 210044, China

3. State Key Joint Laboratory of Environment Simulation and Pollution Control, School of Environment, Tsinghua University, Beijing 100084, China

Abstract: Organic aerosol (OA) makes up a substantial fraction of atmospheric particulate matter that exerts tremendous impacts on air quality, climate, and human health. Yet current chemical transport models fail to reproduce both the concentrations and temporal variations of OA, especially the secondary organic aerosol (SOA), hindering the identification of major contribution sources. One possibility is that precursors that are not yet included in the model exist, and intermediate-volatility and semi-volatile organic compounds (I/SVOCs) are advocated to be one of them. Herein, we established a high-resolution emission inventory of I/SVOCs and by incorporating it into the CMAQ model, concentrations, temporal variations, and spatial distributions of POA and SOA originated from different sources in the Yangtze River Delta (YRD) region of China were simulated. Compared with the comprehensive observation data obtained in the region, i.e., volatile organic compounds (VOCs), organic carbon (OC), primary organic aerosol (POA) and SOA, significant model improvements in the

---

[*] Correspondence to C. Huang (huangc@saes.sh.cn)

simulations of different OA components were demonstrated. Furthermore, spatial and seasonal variations of different source contributions to OA production were identified. We found cooking emissions are predominant sources of POA in the densely populated urban area of the region. I/SVOC emissions from industrial sources are dominant contributors to the SOA formation, followed by those from mobile sources. While the former concentrated in eastern, central, and northern YRD, the latter mainly focused on the urban area. Our results indicate that future control measures should be specifically tailored on intraregional scale based on the different source characteristics to achieve the national goal of continuous improvement in air quality. In addition, local source profiles and emission factors of I/SVOCs as well as SOA formation mechanisms in model framework are urgently needed to be updated to further improve the model performance and thus the accuracy of source identifications.

Key words: semi-volatile and intermediate volatility organic compounds; secondary organic aerosol; emission inventory; source contribution; model simulation

1. Introduction

Organic aerosol (OA) contributes a large fraction (20 to 90%) of atmospheric submicron aerosol (Zhang et al., 2007; Jimenez et al., 2009) and has negative impacts on air quality, climate (Shrivastava et al., 2017), and human health (Nault et al., 2021). OA is composed of primary organic aerosol (POA) directly emitted from fossil fuel combustion, biomass burning, and other sources, as well as secondary organic aerosol (SOA) formed through the atmospheric oxidation of gas-phase species emitted from a wide range of biogenic and anthropogenic sources (Hallquist et al., 2009). Understanding and identifying the origins of OA is therefore important for elucidating their health and climate effects and establishing effective mitigation policies. However, OA is a dynamic system driven by the gas-particle partitioning of organic vapors and particulate organic material, i.e. POA and SOA, and continuously evolves upon atmospheric oxidation (Robinson et al., 2007; Donahue et al., 2009; Zhao et al., 2013; Jathar et al., 2014). It is challenging to constrain the abundance of OA precursors and

54   to identify key sources.

55   Great efforts have been made in the identification of OA sources through source

56   apportionment of the measured OA components, such as positive matrix factorization

57   (PMF) (Zhang et al., 2011), chemical mass balance (CMB) model (Zheng et al., 2002)

58   or multilinear engine (ME-2) (Canonaco et al., 2013). The Aerodyne high-resolution

59   time-of-flight aerosol mass spectrometer (AMS), has been proven to be a powerful tool

60   in quantification and chemical characterization of different OA components in real-time

61   (Canagaratna et al., 2007). Coupled with PMF analysis, AMS measurements allow for

62   the deconvolution of physically meaningful OA factors. Commonly retrieved factors

63   include three POA sources, i.e. hydrocarbon-like OA (HOA) related to fossil fuel

64   combustion, biomass burning OA (BBOA), and cooking-related OA (COA), as well as

65   two SOA components, i.e. less oxidized oxygenated OA (LO-OOA) and more oxidized

66   oxygenated OA (MO-OOA) (Hayes et al., 2013; Crippa et al., 2014; Sun et al., 2014;

67   Li et al., 2017). Combining offline AMS and radiocarbon (^{14}C) measurements, Huang

68   et al. (2014) also identified the contributions of fossil and non-fossil sources to SOA.

69   Attempts have been made in subsequent studies by coupling the AMS measurement

70   with a suite of comprehensive and collocated SOA tracer measurements to distinguish

71   biogenic and major anthropogenic SOA sources, such as traffic and cooking emissions

72   (Xu et al., 2015; Zhang et al., 2018; Zhu et al., 2020; Huang et al., 2021a). However,

73   due to the complex OA composition and variety of emission sources, further

74   deconvolution on the contributions of different sources to OA production is challenging.

75   Besides field measurements, air quality modeling is another widespread technique,

76   which has advantages for regional-scale OA source apportionment with higher temporal

77   and spatial resolution. However, the model simulated SOA concentration still has large

78   gaps with that measured in the atmosphere. The volatility basis set (VBS) scheme is

79   therefore developed, which lumps organic precursors as well as their oxidation products

80   into different volatility bins. Upon atmospheric aging, the volatility of these compounds

81   evolves due to the processes such as functionalization and fragmentation, which can be

82   accounted for in the models by shifting the volatility bins of these compounds (Donahue

83   et al., 2006). It has been widely reported that coupling VBS scheme with air quality

84   models can improve the model performance on SOA simulation (Tsimpidi et al., 2010;

85   Koo et al., 2014; woody et al., 2016; Zhao et al., 2016a; Yang et al., 2019). However,

86   there are still some shortcomings in the modeling of OA with the VBS, for example the

87   lack of representation of the hydrophilic properties of OA, which assumes SOA

88   condenses onto an organic phase, whereas SOA may also condense on an aqueous phase

89   (Kim et al., 2011). Another important constraint is the underestimation of intermediate-

90   volatility organic compounds (IVOCs) and semi-volatile organic compounds (SVOCs)

91   emissions in the models, which potentially have substantial contributions to SOA

92   budget owing to their high SOA yields (Presto et al., 2009; Tkacik et al., 2012; Zhao et

93   al., 2014; Liggio et al., 2016). IVOCs refer to organic compounds with effective

94   saturation concentrations (C*) between 10^3 to 10^6 μg·m^{-3} at 298 K and 1 atm, while

95   SVOCs refer to organic compounds with C* between 10^{-1} to 10^3 μg·m^{-3} at 298 K and 1

96   atm (Robinson et al., 2007).

97   I/SVOC emission inventories have been developed and applied into air quality

98   models over the past decade. Most of them were estimated by applying different scaling

99   factors based on their relationship with POA, volatile organic compounds (VOCs), or

100   some proxies like naphthalene (Pye and Seinfeld, 2010; Shrivastava et al., 2011; Jathar

101   et al., 2017; Wu et al., 2019, 2021; Li et al., 2020, 2022; Ling et al., 2022). Yet in

102   practice, a same scaling factor was applied to most of the sources in previous studies

103   due to the lack of measurements on I/SVOC emission factors. For example, except

104   biomass burning (0.75–1.5), Wu et al. (2019) utilized scaling factors of 8–30 for all of

105   the other emission source categories, which was estimated based on the measurements

106   of on-road mobile source. Li et al. (2020) assumed scaling factors of 1.5 for on-road

107   mobile source, and 0.34–1.5 for the other sources, such as industrial and residential

108   sources, which were much lower than the estimations in Wu et al. (2020). Huang et al.

109   (2021) have tried emission factor method to quantify the I/SVOC emissions, yet the

4

110 results were 60% lower than the scaling factor method, far from catching the measured

111 amount of SOA. Obviously, roughly estimating I/SVOC emissions using one or two

112 emission profiles as surrogates for all emission sources will create large uncertainties.

113   Recent studies have successively determined the volatility distribution, chemical

114 composition, and emission factors of I/SVOCs from mobile sources, including gasoline

115 and diesel vehicles, non-road diesel machinery, marine vessel, and aircraft (Presto et al.,

116 2011; Cross et al., 2013; Zhao et al., 2015, 2016b; Huang et al., 2018; Qi et al., 2019;

117 Drozd et al., 2019). I/SVOC emission profiles have been reported for nonmobile-

118 sources as well, including coal combustion, wood-burning, cooking, fuel evaporation,

119 and industrial and residential volatile chemical products (Huffman et al., 2009; Gentner

120 et al., 2012; May et al., 2013; Koss et al., 2018; McDonald et al., 2018; Cai et al., 2019;

121 Drozd et al., 2021), making the quantification of I/SVOC emissions and their

122 involvement in air quality models possible.

123   In China, SOA has been emerging as an important contributor to air pollution.

124 Field observations reveal that OA contributes significantly (30%) to the $PM_{2.5}$

125 concentrations in most parts of China (Tao et al., 2017; Liu et al., 2018b), among which

126 the SOA contributes up to 80% of OA during haze pollution (Huang et al., 2014; Ming

127 et al., 2017; Li et al., 2021). SOA formation in China has already been examined in

128 several modeling studies. They found that by considering the POA aging and I/SVOCs

129 oxidation in the models, which is realized by the coupling of VBS scheme, the

130 formation and evolution of SOA can be much better simulated compared to the results

131 of the two-product SOA modeling framework (Zhao et al., 2016a; Wu et al., 2019; Li

132 et al., 2020; Yao et al., 2020; Huang et al., 2021). Chang et al. (2022) developed a full-

133 volatility organic emission inventory with source-specific I/SVOC emission profiles for

134 China, which have greatly improved the model performance on SOA concentrations.

135 However, large gaps still exist between the observed and modeled SOA. Studies on

136 high-resolution I/SVOC emission inventory for more specific sources are highly needed.

137   In this study, taking the Yangtze River Delta (YRD) region, including Jiangsu,

138 Zhejiang, Anhui provinces and Shanghai city, as a pilot, we established a high-

139 resolution source specific I/SVOC emission inventory. We then applied the established

140 inventory into CMAQ v5.3 to evaluate the contributions of I/SVOC emissions to SOA

141 formation by comparing the results with the observation data collected in the region.

142 Furthermore, we also run the model in different scenarios to quantify the seasonal

143 contributions of different sources to POA and SOA formation in the YRD region.

144 **2. Materials and methods**

145 2.1 I/SVOC emission inventory

146 I/SVOCs commonly exist in both gas- and particle-phase in the atmosphere.

147 Previous studies usually used POA scaling factors to estimate the I/SVOC emissions,

148 which may lead to large uncertainties in the estimation of gas-phase organic compound-

149 dominated sources, like oil refinery, chemical production, and industrial solvent-use.

150 Herein, we compiled both gas-phase I/SVOCs (I/SVOCs-G) and particle-phase

151 I/SVOCs (I/SVOCs-P) emission inventories and incorporate them into the model.

152 Detailed process of the inventories is as follows.

153 (1) Source classification: To refine the I/SVOC emissions from different sources,

154 we divided the sources into five major categories and then further grouped them into

155 21 sub-categories. The major categories include industrial process sources, industrial

156 solvent-use sources, mobile sources, residential sources, and agricultural sources. As

157 shown in Table S1, the industrial process sources include the sectors such as oil refinery,

158 chemical production, and pulp and paper production; Industrial solvent-use sources

159 include textile, leather tanning, timber processing, and various industrial volatile

160 chemical products use; Mobile sources include gasoline and diesel vehicle emissions,

161 fuel evaporation, diesel machinery, marine vessel, and aircraft; Residential sources

162 include coal combustion, residential solvent-use, and cooking emissions; Agricultural

163 source is specifically referred to biomass burning in household stoves, and open burning

164 was not included in this study.

165 (2) Emission estimation: I/SVOCs-G emissions for each specific source were

166 estimated by the ratios of total I/SVOC components to anthropogenic VOC (AVOC)

167 components (I/SVOCs-to-VOCs). Similarly, I/SVOCs-P emissions were estimated by

168 the ratios of total particle-phase I/SVOC components to POA (I/SVOCs-to-POA). The

169 I/SVOCs-G-to-VOCs and I/SVOCs-P-to-POA ratios for each source were determined

170 according to their fractions of total I/SVOC species in VOC and POA emissions. Then

171 we grouped different I/SVOC species into lumped I/SVOC bins based on their C* to

172 determine the volatility distributions of each source. The I/SVOCs-G emissions were

173 distributed into four lumped aliphatic IVOC bins across the volatility basis set from

174 $C*=10^3$ to 10^6 $\mu g \cdot m^{-3}$, two aromatic IVOC bins with the $C*=10^5$ and 10^6 $\mu g \cdot m^{-3}$, and

175 four lumped SVOC bins with C* from 10^{-1} and 10^2 $\mu g \cdot m^{-3}$. The I/SVOCs-P emissions

176 were distributed into five bins spanning C* from 10^{-1} and 10^3 $\mu g \cdot m^{-3}$. Source profiles

177 of I/SVOC species for different sources were referenced from the results in previous

178 studies. Table S1 and S2 show the I/SVOCs-G-to-VOCs and I/SVOCs-P-to-POA ratios

179 for each specific source and their references. For industrial process, industrial solvent-

180 use, and residential solvent-use sources, only I/SVOCs-G emissions were considered.

181 Their I/SVOCs-G-to-VOCs ratios and emission profiles were derived from the latest

182 version of SPECIATE 5.1 database (US EPA, 2021). For gasoline and diesel vehicles,

183 the I/SVOCs-G-to-VOCs and I/SVOCs-P-to-POA ratios and emission profiles were

184 referenced from a new mobile-source parameterization recommended by Lu et al.

185 (2020). Those of diesel machinery, marine vessel, and residential coal combustion were

186 determined by recent measurement results in China (Qi et al., 2019; Huang et al., 2018;

187 Cai et al., 2019). The I/SVOCs-G-to-VOCs ratios and profiles of cooking and biomass

188 burning emissions were derived from SPECIATE 5.1 database, while their particle-

189 phase ratios and profiles were referenced from two previous studies (May et al., 2013;

190 Louvaris et al., 2017). Table S1 and S2 show the I/SVOCs-G-to-VOCs and I/SVOCs-

191 P-to-POA ratios and their emission profiles of each specific source. The base emissions

192 of AVOCs and POA (See Table S3) were taken from a high-resolution emission

193 inventory for the year of 2017 developed in our previous study (An et al., 2021).

194   (3) Model input: Before being input into the model, the estimated I/SVOC-G and

195   I/SVOC-P emissions were summed and then redistributed according to their phase

196   equilibrium under the actual atmospheric state. The formula of phase equilibrium is

197   shown in Equation (1).

198    $$F_{\mathrm{p}} = \frac{C_{\mathrm{OA}}}{C_{\mathrm{OA}} + C^*}$$ (1)

199   Where, F_{p} is the fraction of particle-phase I/SVOC emissions for each volatility bin.

200   C_{OA} represents the OA concentration in the atmosphere. We assumed it to be 10 µg·m⁻

201   ³ in this study. C^* is the effective saturation concentration of each volatility bin. After

202   redistribution, the I/SVOC emissions for each source category were allocated into 4 km

203   × 4 km grids and hourly temporal profiles using the same method as the criteria

204   pollutants.

205   2.2 Model configuration

206   We used Community Modeling and Analysis System (CMAQ version 5.3.2) to

207   simulate the concentrations of air pollutants. The domain of the simulation is presented

208   in Figure 1. The simulations were conducted for three nested grids with horizontal

209   resolution of 36 km (D1), 12 km (D2) and 4 km (D3), respectively. D1 covers most of

210   China and the surrounding countries including Japan and South Korea; D2 covers

211   eastern China and D3 covers the entire YRD region and its surrounding land and waters.

212   Meteorological fields were provided by the Weather Research and Forecasting

213   (WRF version 3.7) model with 27 vertical layers extending to the tropopause (100 hpa).

214   The initial and boundary conditions (ICs, BCs) in the WRF were based on the 1° × 1°

215   reanalysis data from the National Centers for Environmental Prediction Final Analysis

216   (NCEP-FNL). Physical options used in the WRF simulation are listed in Table S4.

217   The   Sparse   Matrix   Operator   Kernel   Emissions   (SMOKE,

218   https://cmascenter.org/smoke) model was applied to process emissions for input to

219   CMAQ. CMAQ version 5.3.2 (https://cmascenter.org/cmaq/) was used to simulate

220   atmospheric pollutants concentrations. ICs and BCs of D1 domain are based on a Model

221   For   Ozone   And   Related   Chemical   Tracers   (MOZART)   global   simulation

222   (https://acom.ucar.edu/wrf-chem/mozart.shtml). For the inner D2 and D3 domain, ICs

223   and BCs are extracted from the simulation results of the outer domains. Options selected

224   for the CMAQ simulations include the SAPRC07 gas phase chemistry, the AERO7

225   aerosol scheme, the Regional Acid Deposition Model (RADM) model aqueous phase

226   chemistry, ISORROPIA inorganic particulate thermodynamics.

227   The emission inventory developed in this study was used to produce the emission

228   system in the YRD region while emissions beyond YRD were supplied by

229   Multiresolution Emission Inventory for China (MEIC-2017, http://meicmodel.org),

230   Shipping Emission Inventory Model (SEIM) (Liu et al., 2016), and the Model Inter-

231   Comparison Study (MIX) emission inventory for 2010 (Li et al., 2017). The I/SVOC

232   emission inventory outside the YRD region was developed by multiplying the VOCs

233   and POA emissions with the average I/SVOCs-G-to-VOCs and I/SVOCs-P-to-POA

234   ratios of major source categories like industry, vehicle, marine vessel, and residential.

235   Biogenic volatile organic compounds (BVOCs) emissions were estimated based on

236   MEGAN (the Model of Emissions of Gases and Aerosols from Nature) version 2.10

237   driving by inputs of the leaf area index (LAI) from MODIS product, plant functional

238   types (PFT) base on remote sensing data, inline coupled emission factors and

239   meteorology simulated by the WRF model. Detail configurations of MEGAN can be

240   obtained from our previous study (Liu et al., 2018a).
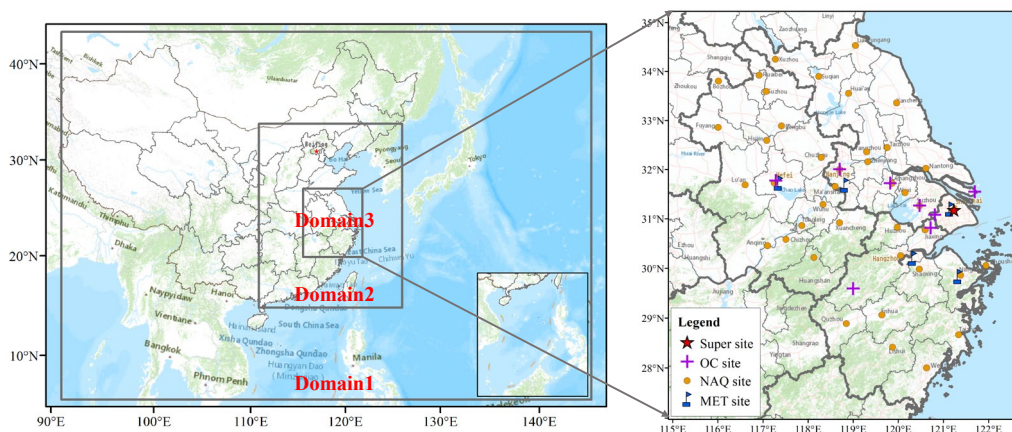
241

242   **Figure 1.** Modeling domain and locations of observation sites. The blue marks are meteorological

monitoring sites. The yellow dots represent the national air quality monitoring sites. The purple crosses are the observation sites with $PM_{2.5}$ chemical composition measurements. The red star represents the observation site of AMS measurement.

SOA formed from I/SVOCs was estimated using the parameterization within the VBS framework in Lu et al. (2020). Specifically, the I/SVOC surrogates react with OH, generating four oxygenated organic species with volatility spanning from $C^* = 10^{-1}$ to 10^2 $\mu g \cdot m^{-3}$, which may exist in both gas and condensed phase. The rate coefficient (i.e., k_{OH}) and product yields (i.e., α_i, i=1, 2, 3, 4) for each primary I/SVOC species were derived based on previous laboratory results (Zhao et al., 2015; Zhao et al., 2016b). Multi-generation oxidation was considered by implementing further oxidation of the vapors from the initial oxidation, which redistributes the mass across the volatility bins of $C^* = 10^{-2}$ to 10^2 $\mu g \cdot m^{-3}$, and thus fragmentation and functionalization were included. Additionally, SOA formation from SVOCs were treated similarly, and more details can be found in Murphy et al. (2017). POA was treated as semivolatile to account for its gas-particle partitioning and ageing process and segregated to several particle species, which varied in their volatility that quantified with the metric $C^* = 10^{-1}$ to 10^3 $\mu g \cdot m^{-3}$ (Donahue et al., 2006). I/SVOCs-P emissions from different sources were then speciated and input as semivolatile accordingly. The remaining POA emissions excluding I/SVOCs-P were treated as nonvolatile POC (primary organic carbon) and PNCOM (primary non-carbon organic matter).

2.3 Model simulations

To investigate the model performance on OA simulations and the contributions of different sources, we set 14 simulation cases using brute-force method (Zhang et al., 2005). Table 1 shows the settings for these 14 cases. First was BASE simulation case, in which the I/SVOC emissions was not included and the POA emissions were treated as non-volatile. The second was the IMPROVE case, which augmented the high-resolution I/SVOC emission inventory established in this study. In addition, the POA emissions in the IMPROVE simulation were split into both non-volatile and semivolatile parts. The non-volatile emissions were obtained by subtracting the

272   I/SVOCs-P from the total POA. The semivolatile emissions, that was I/SVOCs-P

273   emissions, were treated with variable gas–particle partitioning and multigenerational

274   aging in this simulation case. We then used the difference between IMPROVE and

275   BASE cases to evaluate the OA contributions from I/SVOC emissions. CASE1 to

276   CASE12 respectively excluded the VOC and I/SVOC emissions from different sources.

277   We used the differences between IMPROVE and CASE1−12 to quantify the

278   contribution of each source to OA concentration.

279   **Table 1.** Settings of simulation cases.

Name	Sources with added I/SVOC emissions
BASE	none
IMPROVE	all
CASE1	all except industrial process
CASE2	all except industrial solvent-use
CASE3	all except mobile sources
CASE4	all except residential sources
CASE5	all except biomass burning
CASE6	all except biogenic sources
CASE7	without VOCs and I/SVOC emissions
CASE8	all except gasoline vehicle
CASE9	all except diesel vehicle
CASE10	all except diesel machinery
CASE11	all except marine vessel
CASE12	all except cooking

280   2.4 Model evaluation

281   To capture the characteristics of OA with different meteorological features in the

282   YRD region, we selected four periods to represent spring (Mar. 15th to Apr. 15th, 2019),

283   summer (Jul. 1st to 31st, 2019), autumn (Oct. 15th to Nov. 15th, 2018), and winter (Dec.

284   1st to 31st, 2018) to conduct the simulations. Evaluations on model performance were

285   made by comparing the simulation results with the observations obtained in the region,

286   including 5 meteorological observation sites, 10 $PM_{2.5}$ chemical composition sites, and

287   41 national air quality monitoring sites, one in each city. The locations of the

288   meteorological and air pollutant observation sites are shown in Figure 1.

289   We also used the observation data of an AMS and a GC-MS/FID system at the

supersite in Shanghai to further verify the model performance on the simulation of POA, SOA, and key VOC precursors. Details of AMS measurements and PMF analysis are provided in our previous study (Huang et al., 2021). A total of 55 PAMS (Photochemical Assessment Monitoring Stations) species were identified by the GC-MS/FID system including 27 alkanes, 11 alkenes, acetylene and 16 aromatics. The supersite was located on the top-floor of an eight-story building in Shanghai Academy of Environmental Sciences (SAES, 31°10' N, 121°25'E), 30 m above the ground. The site was in a typical residential and commercial area with significant influence from traffic emission. Several petrochemical and chemical industrial factories sit around 50 km away from the site to the south and southwest.

Model performance in simulation of meteorological parameters and major criteria air pollutants are summarized in Table S5 and S6. The mean bias (MB), mean gross error (MGE), root-mean-square error (RMSE), and index of agreement (IOA) of temperature, humidity, wind speed, and wind direction in each season are within the criteria recommended by Emery et al. (2001). Although the temperature in summer and winter, and wind speed in autumn and winter were slightly overestimated, their MGE and IOA values are within the uncertainties as recommended in Emery et al. (2001).

For the simulation of major criteria air pollutants, both mean fractional bias (MFB) and mean fractional error (MFE) of all pollutants met the criteria recommended by Boylan and Russell (2006). Since the addition of I/SVOC emissions would change the $PM_{2.5}$ simulation results, we thus presented the statistical results for both BASE and IMPROVE cases in the Table S6. The modeled SO_2 was slightly overestimated, which is likely due to the faster than expected reduction of SO_2 emissions, resulting in overestimation of SO_2 emissions in the emission inventory. On the contrast, the modeled NO_2 were underestimated in spring, autumn, and winter, likely due to the overestimation of wind speed in these seasons. The modeled O_3 and $PM_{2.5}$ were slightly overestimated in the IMPROVE simulation case. Overall, the simulated meteorological parameters and major criteria air pollutants are consistent with the observations.

3. Results and discussion

3.1 I/SVOC emission inventory

3.1.1 Source-specific I/SVOC emissions

Table 2 shows the I/SVOCs-G and I/SVOCs-P emission inventories for detailed source category for year 2017 in the YRD region. The total I/SVOC-G emission in the YRD region was 1148.42 Gg in 2017, lower than that in Wu et al. (2021) of 1360 Gg, but higher than the estimate in Huang et al. (2021b) of 730 Gg. We found industrial solvent-use was the largest contributor (483.64 Gg, 42.11%) of total S/IVOCs-G emissions, followed by industrial process sources (244.65 Gg, 21.30%), mobile source (344.31 Gg, 29.98%), residential source (62.23 Gg, 5.42%), and agriculture source (13.58 Gg, 1.18%). Specifically, chemical production, textile, and solvent-based coating were major sectors of I/SVOCs-G emissions in the YRD region, accounting for 20.80%, 19.51%, and 15.07% of the total I/SVOCs-G emission, and their contributions to AVOC emissions were 20.70%, 2.22%, and 23.42%, respectively (See Table S3). It is interesting to note that the I/SVOCs-to-VOCs ratios are largely different for different sources. For example, the textile industry only accounted for 2.22% of the total AVOC emissions in the YRD region but contributed to 19.51% of the I/SVOC-G emissions due to its higher I/SVOCs-to-VOCs ratio (2.473). Another example is water-based coatings, whose VOC emissions were approximately 10.2% of solvent-based coatings, while their I/SVOC emissions were 29.1% of those from solvent-based coatings. These findings indicate that reductions in VOC emissions not necessarily corresponds to the simultaneous reductions in I/SVOCs emissions and subsequent SOA formation, which should be considered in future control strategies. (Yuan et al., 2010).

For I/SVOCs-G emission of mobile origin, the major contributors were gasoline vehicle, diesel vehicle, and non-road diesel machinery, accounting for 13.64%, 11.66%, and 2.11%, respectively. The total I/SVOCs-G emissions from gasoline and diesel vehicles were 290.57 Gg, much higher than the results reported in Liu et al. (2017) (29.58 Gg) and Huang et al. (2021b) (16.0 Gg) using the emission factor method, which

346 likely underestimates the emission factors of I/SVOCs due to the lack of localized

347 emission factors. Our tunnel experiment results show that the average IVOCs emission

348 factors of gasoline and diesel vehicles were 15.3 mg·km^{-1} and 219.8 mg·km^{-1} (Tang et

349 al., 2021), which were significantly higher than those used in the above studies (Liu et

350 al., 2017; Huang et al., 2021b). More comprehensive localized emission measurements

351 are advocated to better constrain the I/SVOC emissions from mobile sources.

352   I/SVOCs-P emissions were 82.96 Gg. The largest contributor of I/SVOCs-P

353 emissions came from cooking emission and diesel vehicle, accounting for 53.24% and

354 11.88% of the total, followed by gasoline vehicle (5.23%), marine vessel (2.66%),

355 diesel machinery (2.54%), and biomass burning (1.75%). Note that the I/SVOCs-P

356 emissions from coal combustion (e.g. power plants, boilers, etc.), other industrial

357 processes, and aircraft were not included in this study. On the one hand, the POA

358 emissions (See Table S3) from these sources were limited, accounting for less than 5%,

359 which could be expected that their I/SVOCs-P emissions were also relatively low. On

360 the other hand, the profiles of I/SVOCs-P components of these sources were still

361 difficult to obtain. More measurements of the I/SVOC emissions from these sources is

362 very necessary in the future.

363 **Table 2.** Source-specific emissions of I/SVOCs for the year 2017 in the YRD region.

Source		I/SVOCs		I/SVOCs-G		I/SVOCs-P	
		Gg	%	Gg	%	Gg	%
Industrial process	Oil refinery	5.63	0.46	5.62	0.49	0.01	0.01
	Chemical production	243.60	19.78	238.91	20.80	4.69	5.65
	Pulp and paper	0.11	0.01	0.11	0.01	0.00	0.00
Industrial solvent-use	Textile	229.78	18.66	224.06	19.51	5.72	6.90
	Leather tanning	3.83	0.31	3.83	0.33	0.00	0.00
	Timber processing	31.08	2.52	31.08	2.71	0.00	0.00
	Furniture coating	1.32	0.11	1.32	0.12	0.00	0.00
	Solvent-based coating	173.02	14.05	173.01	15.07	0.00	0.00
	Water-based coating	50.32	4.09	50.32	4.38	0.01	0.01
	Dry cleaning	0.02	0.00	0.02	0.00	0.00	0.00
	Paint remover	0.01	0.00	0.01	0.00	0.00	0.00
Mobile source	Gasoline vehicle	161.01	13.08	156.67	13.64	4.34	5.23

	Diesel vehicle	143.76	11.67	133.90	11.66	9.86	11.88
	Fuel evaporation	0.69	0.06	0.69	0.06	0.00	0.00
	Diesel machinery	49.62	4.03	47.51	4.14	2.11	2.54
	Marine vessel	7.12	0.58	4.91	0.43	2.21	2.66
	Aircraft	0.64	0.05	0.64	0.06	0.00	0.00
	Coal combustion	2.73	0.22	2.73	0.24	0.00	0.00
Residential source	Residential solvent-use	35.29	2.87	35.20	3.07	0.09	0.11
	Cooking	76.77	6.23	24.30	2.12	52.46	63.24
Agriculture source	Biomass burning	15.04	1.22	13.58	1.18	1.45	1.75
	Total	1231.38	100.00	1148.42	100.00	82.96	100.00

3.1.2 Volatility distributions of I/SVOCs

Figure 2 shows the volatility distribution of I/SVOC emissions from different sources as well as their gas-particle distributions. The I/SVOC emissions generally showed an increasing trend with the increase of volatility. As shown in Figure 2(a), IVOC emissions (logC* bins at 3−6) accounted for 86% of the total I/SVOCs emissions, overwhelmingly dominated by industrial process and mobile sources. SVOCs (logC* bins at 0−2) and low-volatile organic compounds (LVOCs, logC* bins at -1) contributed to 11% and 3% of the total I/SVOCs emissions. In terms of the contributing sectors, mobile sources, industrial process, and solvent-use dominated the total I/SVOC emissions. While the IVOCs were equally contributed by above-listed three sources, residential and mobile sources dominated the SVOCs and LVOCs emissions.

We further investigated the contributions of different volatility bins to each source category. The mobile source was dominated by IVOC emission (88%). Note that IVOCs in vehicle exhaust are dominated by aromatics, which have faster OH reaction rates and higher SOA yields compared to aliphatics in the same volatility bin (Zhao et al., 2016b; Drozd et al., 2019). Lu et al. (2020) therefore defined two additional lumped IVOC species with logC* bins at 5 and 6 to account for the aromatic IVOCs in vehicle exhaust according to the measurements in previous studies (Zhao et al., 2015; Zhao et al., 2016b). Here in this study, we also split the aromatic IVOC emissions from mobile sources and found that aromatic IVOCs accounted for 23% of the total I/SVOC emissions from the mobile source. The industrial process and solvent-use sources were

also dominated by IVOC emissions, accounting for 81% and 97%, respectively. The volatility distribution of residential sources was relatively uniform, with IVOCs, SVOCs and LVOCs accounting for 40%, 30%, and 30%. Agricultural (i.e., biomass burning) sources were more concentrated in IVOCs, accounting for 76%, while SVOCs accounted for 24%. It should be noted that other than mobile sources, the emission profiles of the other sources were mainly derived from SPECIATE 5.1 database (US EPA, 2021) in this study, which may be inconsistent with real-world emissions in China. To further reduce the uncertainty in the I/SVOC emission inventory, measurements of I/SVOC emissions from different local sources are therefore important and urgently needed in the future.
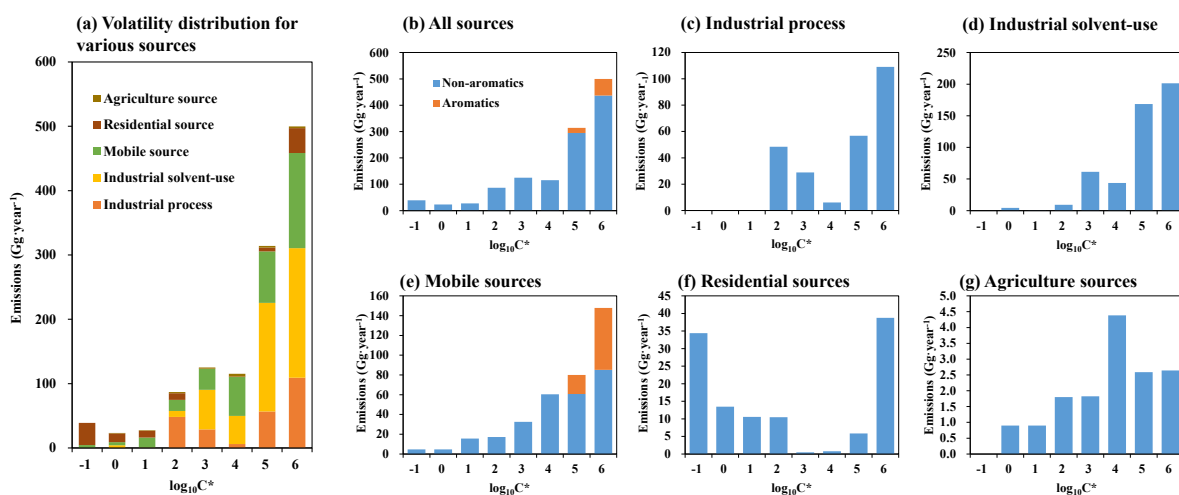
**Figure 2.** Volatility distributions of I/SVOCs emitted from different sources in the YRD region.

3.1.3 Spatial distributions of I/SVOC emissions in YRD region

Figure 3 compares the spatial distributions of AVOC, IVOC, SVOC, and LVOC emissions in the YRD region. The IVOC, SVOC, and LVOC emissions were largely concentrated in city clusters in eastern YRD, and hotspots can also be observed in the northern agglomerations. The distributions of I/S/LVOC emissions were generally consistent with that of the AVOC emissions in the region. Compared to the spatial distributions of I/S/LVOC emissions in Chang et al. (2022), our emissions had similar spatial distributions but at a higher resolution. Emission hotspots in urban areas can be captured more clearly in this study, which will help improve the simulation in urban

406　areas.

407　　　Figure 4 shows the spatial distributions of source-specific I/SVOC emissions in

408　the YRD region. There were considerable differences in the spatial distributions of

409　I/SVOC emissions from different sources. The I/SVOC emissions from industrial

410　sources (including industrial process and industrial solvent-use) were mainly

411　concentrated in the eastern urban agglomeration, which was related to the developed

412　industrial activities in the region. The I/SVOC emissions from mobile and residential

413　sources clustered into multiple hotspots in urban areas, while emissions from

414　agricultural sources were mainly distributed in northern YRD, where frequent

415　agricultural activities exist.

416　　　We also compare the spatial distributions of I/SVOC emissions with those of POA

417　and BVOCs. We found that POA emissions were more concentrated in urban centers

418　associated with mobile and residential sources (See Figure S1). BVOC emissions in the

419　YRD region were mainly distributed in the southern area, where AVOC and IVOC

420　emissions were relatively low. The difference in the spatial distributions of I/SVOC,

421　AVOC, BVOC, and POA emissions implies that the sources of organic components in

422　different areas of the region are quite different, which will be discussed in the following

423　sections.
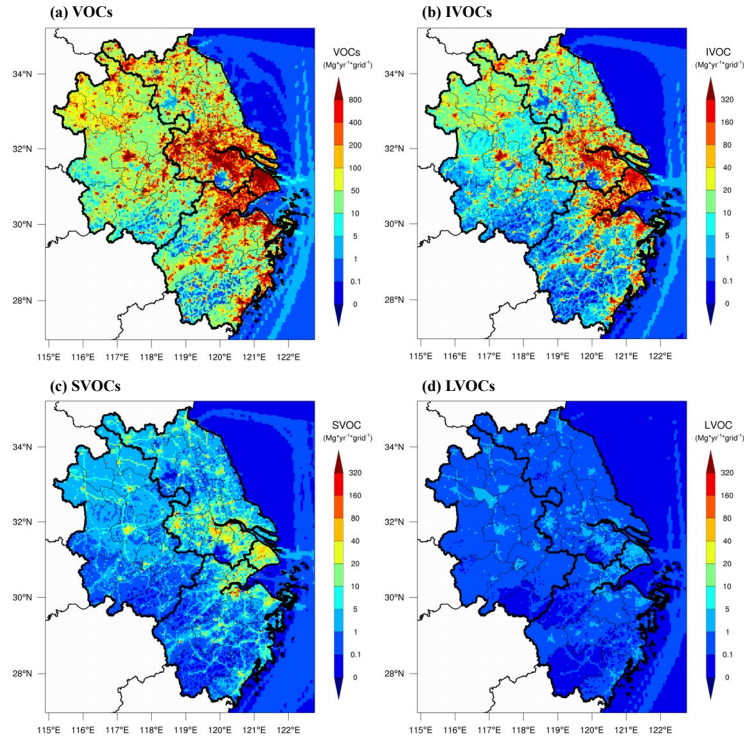
Figure 3. Spatial distributions of anthropogenic VOC, IVOC, SVOC, and LVOC emissions in the YRD region for the year 2017.
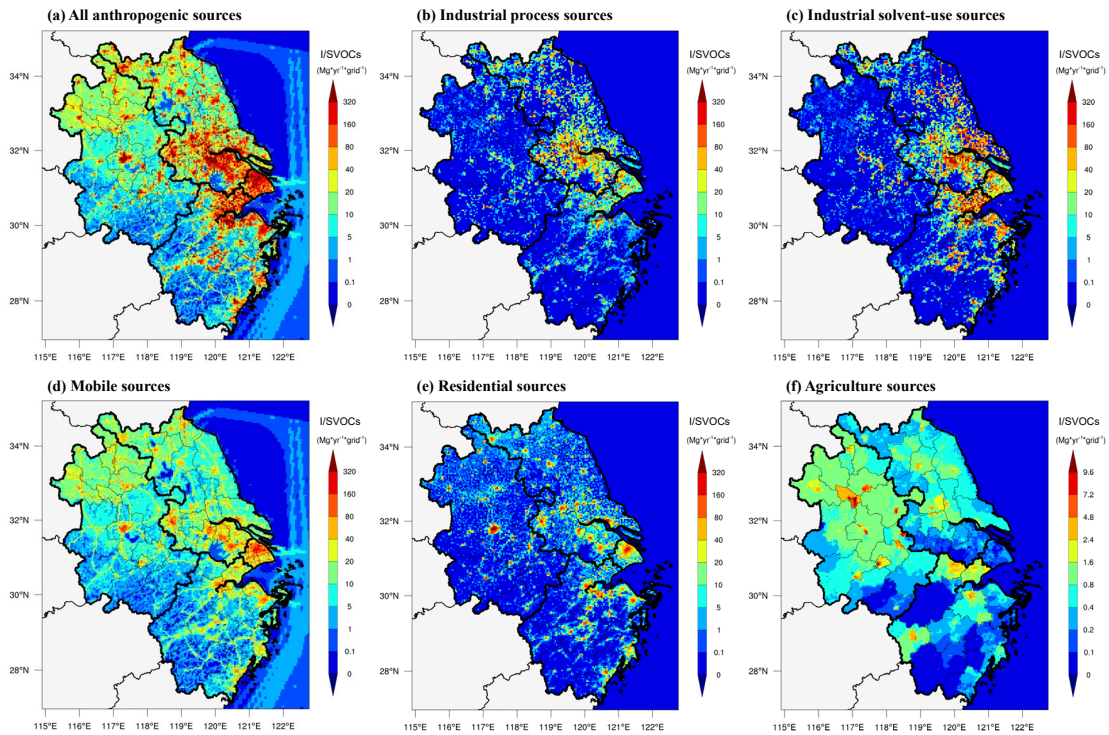
Figure 4. Spatial distributions of I/SVOC emissions from different source categories in the YRD region for the year 2017.

430   3.2 Comparison between model simulation and observation

431   3.2.1 Simulation results of VOCs and IVOCs

432   Since model performance on the simulation of VOCs are critical for SOA

433   estimation, we first compare the modeled concentrations of VOCs with those of the

434   measured at the SAES supersite for several aromatic VOCs, including benzene, toluene,

435   and m-/p-/o-xylenes. As shown in Figure S2, the model simulation was able to capture

436   the hourly variations of these species measured, with Pearson correlation coefficients

437   (r) of 0.54−0.65, 0.45−0.60, 0.54−0.69 for toluene, xylene, and benzene respectively.

438   Although the simulation results of toluene were 28% lower and xylene and benzene

439   were 41% and 22% higher than those of the measured, the model results are within the

440   uncertainties. Overall, the simulation results of the VOC species showed good

441   agreements with the observations, which could be further used for the model simulation

442   of SOA formation.

443   Long-term continuous observations of I/SVOC concentrations were sparse, so the

444   simulation results of IVOCs were compared with those obtained from offline

445   measurements reported in our previous studies (Li et al., 2019; Ren et al., 2020). The

446   reported IVOC concentrations (sum of gas- and particle-phase concentrations) in

447   summer and winter Shanghai in 2018 respectively varied between 1.5−17.2 and

448   2.2−43.1 μg·m^{-3} with average concentrations of 6.8 ± 3.7 and 18.2 ± 11.0 μg·m^{-3}. In

449   this study, our modeled average concentrations of IVOCs in spring, summer, autumn,

450   and winter at the SAES supersite in Shanghai were 12.8 ± 5.6, 9.0 ± 3.2, 12.2 ± 5.2,

451   and 12.4 ± 7.6 μg·m^{-3}, respectively. Although there was still a deviation of 20%−30%

452   between the simulation and observation, not to mention the diurnal patterns and spatial

453   distributions also remained unknown, the simulation results are at least comparable to

454   those of the measured concentrations, suggesting the modeled I/SVOCs is appropriate

455   to be used in the estimation of SOA production from different sources. Continuous long-

456   term measurements of I/SVOC at multiple locations are strongly recommended in the

457   future to improve the model performance and reduce the uncertainties in SOA

458   estimation.

459   3.2.1 Simulation results of OA concentrations

460   Figure 5 presents the OA concentrations originated from different sources,

461   including POA and SOA formed from AVOCs, BVOCs, and I/SVOCs, in four seasons

462   in YRD from both BASE and IMPROVE simulations. Here we used the average of the

463   modeled concentrations at 41 national air quality monitoring sites (See the yellow dots

464   in Figure 1) to represent the regional average. The regional average concentration of

465   OA (8.75 $\mu g \cdot m^{-3}$) in the IMPROVE simulation was 22% higher than that from BASE

466   simulation (7.17 $\mu g \cdot m^{-3}$) due to the involvement of I/SVOCs in the IMPROVE

467   simulation.

468   The seasonal average concentration of POA was 5.5 $\mu g \cdot m^{-3}$ in the BASE case, with

469   the lowest in summer (3.8 $\mu g \cdot m^{-3}$) and the highest in winter (6.9 $\mu g \cdot m^{-3}$). High POA

470   concentrations in winter was mainly induced by the stagnant meteorological conditions

471   such as low wind speed and boundary layer height, and vice versa in summer. For the

472   spatial distributions as presented in Figure 6, POA concentrations in northern YRD were

473   high and mainly concentrated in urban areas, which was consistent with the

474   distributions of POA emissions (Figure S1). The POA concentrations in the IMPROVE

475   simulation decreased by 12%−20% compared with the BASE case. In the IMPROVE

476   simulation, the POA was treated as semi-volatile, where gas–particle partitioning and

477   multigeneration oxidation were considered (Murphy et al., 2017). Entering into the

478   atmosphere, more semi-volatile compounds evaporated into gas-phase and then

479   generated SOA through multigeneration oxidation, which reduced the POA

480   concentrations relatively.

481   The seasonal average concentration of AVSOA in the BASE case was only 0.22

482    $\mu g \cdot m^{-3}$. The average AVSOA concentration in the IMPROVE case increased by 17%

483   compared with the BASE case due to higher OA loading. Nonetheless, AVSOA still

484   exhibited very limited contribution to the regional OA concentration, whereas average

485   concentration of BVOC derived SOA (BVSOA, 1.7 $\mu g \cdot m^{-3}$ in the IMPROVE

486   simulation case) was much higher. Also, evident seasonal variations were observed for

487   BVSOA, with the highest in summer (2.27 $\mu g \cdot m^{-3}$), followed by spring (1.65 $\mu g \cdot m^{-3}$),

488   autumn (1.62 $\mu g \cdot m^{-3}$), and winter (1.11 $\mu g \cdot m^{-3}$). Hotspots of BVSOA concentrations

489   were concentrated in the western and southern YRD. The observed seasonal variations

490   and spatial distributions of BVOC derived SOA were consistent with those of the

491   BVOC emissions in YRD (Liu et al., 2018a).

492   The average concentration of I/SVOC derived SOA (I/SVSOA) in IMPROVE

493   simulation was 2.18 $\mu g \cdot m^{-3}$, with the highest in spring (2.66 $\mu g \cdot m^{-3}$) and the lowest in

494   summer (1.79 $\mu g \cdot m^{-3}$), which was a combined effect of emission, oxidation and

495   meteorological conditions. For example, Qin et al. (2022) suggested that in spring the

496   enhanced solar radiation and OH oxidation potentially promote the secondary

497   conversion from I/SVOCs to SOA. The low concentration in summer was likely due to

498   the better meteorological conditions than the other seasons. By incorporating I/SVOC

499   emissions into the IMPROVE simulation, the modeled average SOA concentration in

500   the region increased from 1.66 (BASE) to 4.10 $\mu g \cdot m^{-3}$; and high concentrations of

501   I/SVSOA were observed in central and northern YRD. Overall, the addition of high-

502   resolution I/SVOC emissions significantly increase the SOA concentration by 148%,

503   which will be further constrained by the observation in next section.

504   To validate the model performance on regional OA simulation, we compared it

505   with the measured concentrations of organic carbon (OC) in $PM_{2.5}$ at multiple sites in

506   the YRD region (Figure S3). Although both BASE and IMPROVE simulations showed

507   good correlations with the observation as shown in Figures S3c, S3f, S3i, and S3l, OC

508   concentrations in IMPROVE simulations in different seasons were all higher than those

509   in the BASE simulations. In the BASE simulation, the modeled OC concentrations of

510   each season only explained 51% to 71% of the observations. With the addition of

511   I/SVOC emissions into IMPROVE simulation, the modeled OC concentrations much

512   better agreed with the observations, with modeled OC increased to 70% to 91% of the

513   observations. Details for the statistical evaluation of model performance on OC in
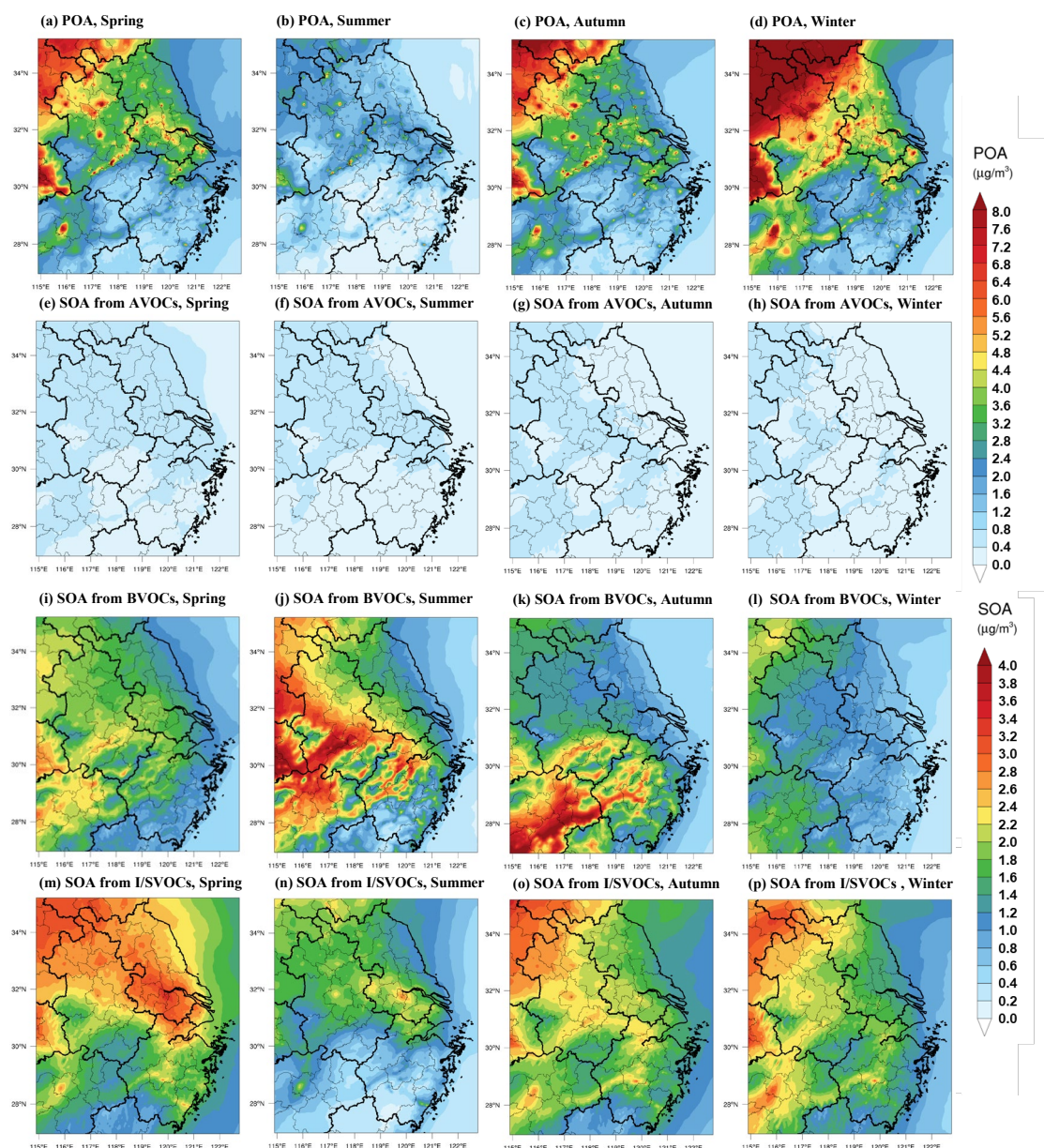
514   BASE and IMPROVE simulations are shown in Table S7.
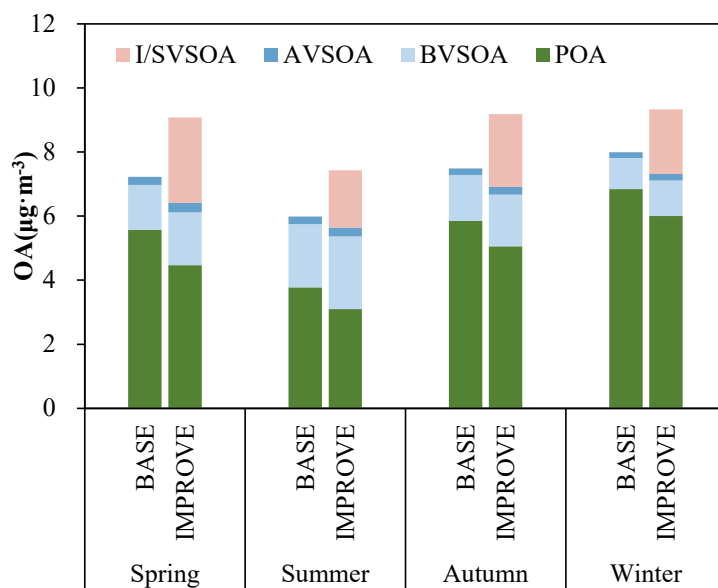
515
516   **Figure 5.** Comparisons of the regional average concentrations of POA and SOA formed from
517   AVOCs, BVOCs, and I/SVOCs in different seasons from the BASE and IMPROVE simulations.

Figure 6. Spatial distributions of modeled POA and SOA formed from AVOCs, BVOCs, and I/SVOCs in different seasons in the IMPROVE simulation.

3.2.2 Temporal variations of OA components: simulation vs. AMS observation

To further validate the model performance on the simulations of POA and SOA, we compared the simulation results with those measured by an AMS at the SAES supersite. Both simulation and observation results were obtained for PM_1 aerosol particles (aerodynamic diameter < 1 μm). Figure 7 shows that the simulation results of POA, SOA and OA were similar to the observation results not only in average concentration levels but also in temporal variations. For POA, the diurnal patterns in

528   the BASE and IMPROVE simulations agree with each other and both can reproduce

529   the observed concentrations. The POA concentrations in the IMPROVE simulation

530   cases decreased by 4%−18% (Figure S4) compared with the BASE case and was closer

531   to the observations. Similar to the observation results, the simulated POA

532   concentrations peaked at noon and early evening, which were mainly contributed by

533   cooking emissions as reported in our previous study (Huang et al., 2021).

534   For SOA, the average concentrations in spring, summer, autumn, and winter in

535   BASE simulation were 1.2, 1.6, 0.8, and 0.7 $\mu g \cdot m^{-3}$, respectively, which were only

536   14%−30% of those observed by the AMS (see Figure S4). The SOA simulation was

537   greatly improved in IMPROVE simulation with the modeled SOA concentrations of 3.8

538   3.7, 2.7, and 2.3 $\mu g \cdot m^{-3}$ in spring, summer, autumn, and winter respectively. The SOA

539   concentrations in IMPROVE simulation were 2.4−3.6 times higher than those in BASE

540   simulation, which is 40% to 72% of the observation, indicating the large contributions

541   of I/SVOCs emissions to SOA production. The IMPROVE simulation also

542   demonstrated improvements in reproducing the temporal variations of SOA, especially

543   during the daytime (Figure 7e−7h). Compared with the BASE simulation, evident

544   increases in SOA concentrations during daytime can be observed in IMPROVE

545   simulation, which agrees better with the observation, likely driven by photochemistry.

546   Although the SOA simulations were improved in all four seasons, best simulation

547   results were found in summer, when both the concentrations and diurnal variations of

548   SOA were well reproduced.

549   While our current results presented great improvements in SOA simulation, gaps

550   were still left between the simulation and observation especially during the nighttime.

551   The main reasons for the discrepancy between the simulated and measured SOA are:

552   (1) I/SVOC emissions from outside of the YRD region might be underestimated due to

553   the lack of detailed base emission inventory, resulting in the corresponding

554   underestimation of the transported SOA, which were prominent especially in autumn,

555   winter and spring in Shanghai; (2) current model simulation only consider the oxidation

processes driven by OH oxidation. However, an increasing body of experimental and observational evidence suggest that heterogeneous and multiphase reactions also played important roles in SOA formation especially during pollution episodes (Guo et al., 2020; Kim et al., 2021). Recent studies also found that nocturnal NO_3 oxidation was also an important route for SOA formation (Yu et al., 2019; Decker et al., 2021). Yet mechanism and parameterizations of these processes remain unclear, making the involvement of these processes in the model difficult.
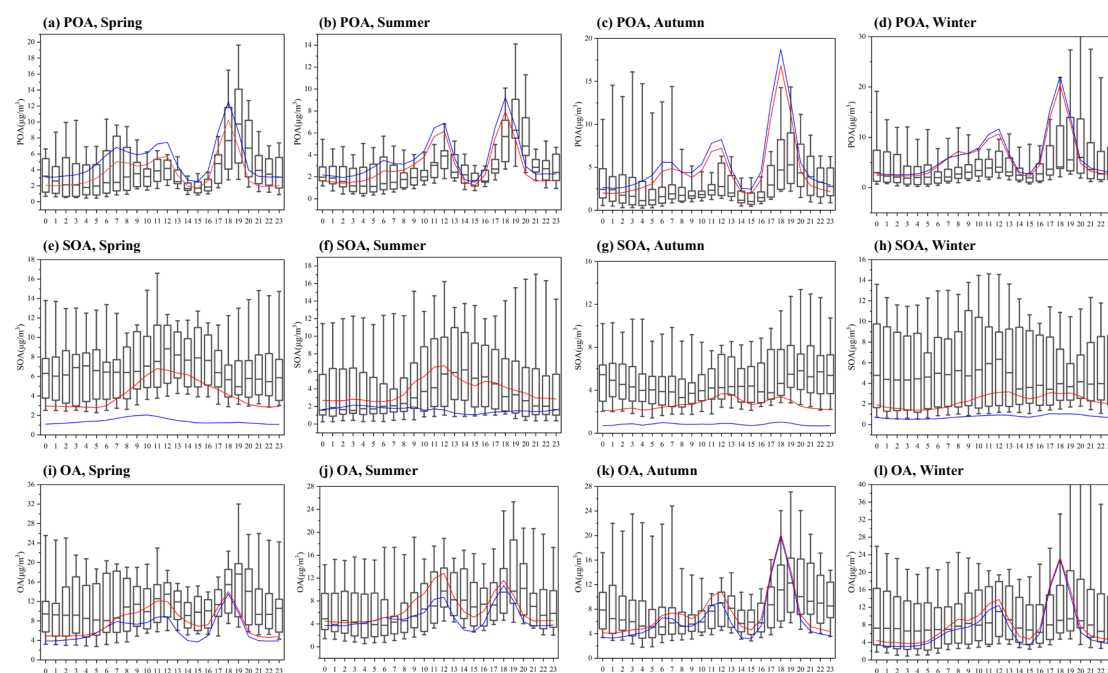
Figure 7. Diurnal patterns of modeled POA, SOA, and OA concentrations in different seasons and their comparisons with the observations at the SAES supersite. The boxplots represent the diurnal patterns of the AMS observations. The blue and red lines respectively represent the diurnal patterns of the simulation results in BASE and IMPROVE cases.

3.3 OA source contributions

3.3.1 POA and SOA sources in the region

Based on the high-resolution I/SVOC emission inventory established in this study, we successfully simulated the POA and SOA concentrations from each source. Table 3 summarizes the regional average concentrations of POA and SOA originated from different sources and their relative contributions. Residential POA dominated the regional OA, with average concentrations ranged from 1.56 to 2.35 μg·m^{-3} in different

seasons, accounting for 19.47%−25.31% of the total OA, among which cooking emission is the dominant source (*ca.* 98%) of residential POA. Other POA sources include industrial, biomass burning, and mobile sources, accounting for 8.02%−8.63%, 4.45%−8.28%, and 5.03%−5.78% of the total OA, respectively. The cumulative fraction of POA in total OA from industrial and mobile sources was 13.44%−14.41%, close to that of HOA (15%) observed by the AMS measurement in Shanghai (Figure S5).

Industrial sources were the main source of SOA in the YRD region, with average SOA concentrations of 0.84−1.21 $\mu g \cdot m^{-3}$ in four seasons, accounting for 8.98%−15.64% of the total OA, among which, industrial process and solvent-use sources had almost equal contributions. Mobile sources were the second largest source of SOA in this region, with an average concentration of 0.31−0.50 $\mu g \cdot m^{-3}$, accounting for 3.36%−6.69% of the total OA. Among them, the source contribution of gasoline vehicles to SOA was 1.77%−3.07%, and that of diesel vehicles was 1.18%−2.55%. BVSOA showed significant seasonal differences with concentrations of 0.88, 1.26, 0.70, and 0.11 $\mu g \cdot m^{-3}$, respectively in spring, summer, autumn, and winter, accounting for 9.64%, 16.94%, 7.60%, and 1.15% of the total OA.

Overall, cooking emission was the major source of POA in YRD, accounting for 19.14%−24.99% of the total OA, which is consistent with our observations in Shanghai (Huang et al., 2021; Zhu et al., 2021). Both simulations and observations demonstrated higher contributions of cooking emission in urban China than those reported overseas (17%–18%) (Chen et al., 2021), which is attributed to the difference between Asian-style and Western-style cooking. The results emphasize that cooking emission has become a non-negligible source of non-fossil carbon in urban areas in eastern China. Contributions from industrial sources were running the second among all sources, accounting for 17.02%−24.12% of OA and 24.7%–26.8% of SOA, which is attributed to the high I/SVOC emissions from industrial sources and is consistent with previous studies (Miao et al., 2021). Other sources mainly include mobile sources (8.76% to

603 11.72% of OA) and biomass burning (5.19%−8.87% of OA). Specifically, diesel and

604 gasoline vehicles were the major contributors among mobile sources, with higher

605 contribution from the former (3.95%−4.66%) than the latter (3.05%−4.02%), followed

606 by diesel machinery (1.32%−2.11%) and marine vessels (0.43%−0.93%). The

607 contribution of biomass burning was highest in winter (8.87%) compared to

608 contributions of 5.19%−7.28% in other seasons and it was even higher than contribution

609 of mobile sources (8.76%) in winter. The remaining 14.54%−35.64% of OA was from

610 super region scale, which represented OA originated from emissions outside the YRD

611 region. Our results were generally similar with those of Chang et al. (2022) for the YRD

612 region. We both found the domestic combustion mainly engaged in cooking emissions

613 had a major contribution to OA. Next was volatile chemical products (VCPs), especially

614 the use of solvents, paints, and adhesives in industrial sector, also made a high

615 contribution. Note that industrial process also took up a high fraction in our OA

616 simulation, while it was lower in Chang et al. (2022)'s study. The difference in I/SVOC

617 emission estimates was the main reason for this divergence. Mobile sources in both

618 studies had similar contributions, which accounted for about 10% to total OA.

619 Comparatively, our source classification was more specific, which will help identify

620 more specific OA sources to design more refined regional control countermeasures.

621 **Table 3.** POA and SOA source contributions of different emission sources in each season in the

622 YRD region.

Sources	Spring		Summer		Autumn		Winter	
	conc.	ratio	conc.	ratio	conc.	ratio	conc.	ratio
	($\mu g \cdot m^{-3}$)	(%)	($\mu g \cdot m^{-3}$)	(%)	($\mu g \cdot m^{-3}$)	(%)	($\mu g \cdot m^{-3}$)	(%)
POA	4.47	49.19	3.09	41.65	5.05	55.06	6.00	64.29
Industrial sources	0.73	8.02	0.63	8.48	0.79	8.63	0.75	8.04
Industrial process	0.61	6.71	0.54	7.27	0.67	7.29	0.63	6.77
Industrial solvent-use	0.12	1.31	0.09	1.20	0.12	1.34	0.12	1.27
Mobile sources	0.49	5.43	0.37	5.03	0.53	5.78	0.50	5.40
Gasoline Vehicles	0.09	1.01	0.07	0.96	0.12	1.32	0.12	1.28
Diesel Vehicles	0.23	2.58	0.16	2.16	0.26	2.79	0.26	2.77
Diesel machinery	0.10	1.06	0.09	1.21	0.10	1.08	0.09	0.95
Marine vessel	0.07	0.78	0.05	0.70	0.05	0.59	0.04	0.39

Residential sources	1.77	19.47	1.56	20.95	2.32	25.31	2.35	25.16
Cooking	1.74	19.14	1.54	20.72	2.29	24.99	2.31	24.77
Other residential	0.03	0.33	0.02	0.23	0.03	0.33	0.04	0.39
Biomass burning	0.60	6.65	0.33	4.45	0.60	6.58	0.77	8.28
Super region	0.87	9.63	0.20	2.75	0.80	8.75	1.62	17.41
SOA	4.61	50.81	4.34	58.35	4.13	44.94	3.33	35.71
Industrial sources	1.21	13.38	1.16	15.64	1.02	11.10	0.84	8.98
Industrial process	0.68	7.53	0.62	8.39	0.61	6.62	0.53	5.64
Industrial solvent-use	0.53	5.84	0.54	7.25	0.41	4.48	0.31	3.34
Mobile sources	0.49	5.45	0.50	6.69	0.43	4.63	0.31	3.36
Gasoline Vehicles	0.25	2.71	0.23	3.07	0.21	2.25	0.16	1.77
Diesel Vehicles	0.18	1.95	0.19	2.50	0.16	1.73	0.11	1.18
Diesel machinery	0.06	0.66	0.07	0.90	0.05	0.56	0.03	0.37
Marine vessel	0.01	0.13	0.02	0.22	0.01	0.09	0.00	0.04
Residential sources	0.42	4.68	0.49	6.54	0.43	4.71	0.32	3.39
Cooking	0.21	2.34	0.29	3.97	0.26	2.78	0.16	1.71
Other residential	0.21	2.34	0.19	2.58	0.18	1.93	0.16	1.68
Biomass burning	0.06	0.63	0.06	0.74	0.05	0.59	0.06	0.60
Biogenic	0.88	9.64	1.26	16.94	0.70	7.60	0.11	1.15
Super region	1.55	17.04	0.88	11.80	1.50	16.30	1.70	18.23

3.3.2 Spatial distributions of SOA originated from different sources

Figure 8 shows the spatial distributions of modeled SOA originated from different sources in each season in YRD region. Note that we only considered the SOA formed from the intraregional VOC and I/SVOC emissions, excluding those transported from the super region. A large spatial variability was observed for the sources of SOA driven by emissions. For example, industrial and mobile SOA concentrated in the eastern and central YRD, where I/SVOC emissions were high (Figure 4). Residential and agricultural SOA presented a more uniform spatial distribution than industrial and mobile SOA, with enhanced formation in central and western YRD (Figures 8i-8l).

Although absolute source-dependent SOA concentrations differ in different seasons, low spatial variabilities were observed for different seasons. Industrial, mobile, and residential sources were the predominant contributors to SOA formation in eastern and central YRD, especially for the area along the Hangzhou Bay and Yangtze River driven by the enhanced I/SVOC emissions. The spatial distributions of BVSOA have

been discussed above and will not be detailed here.
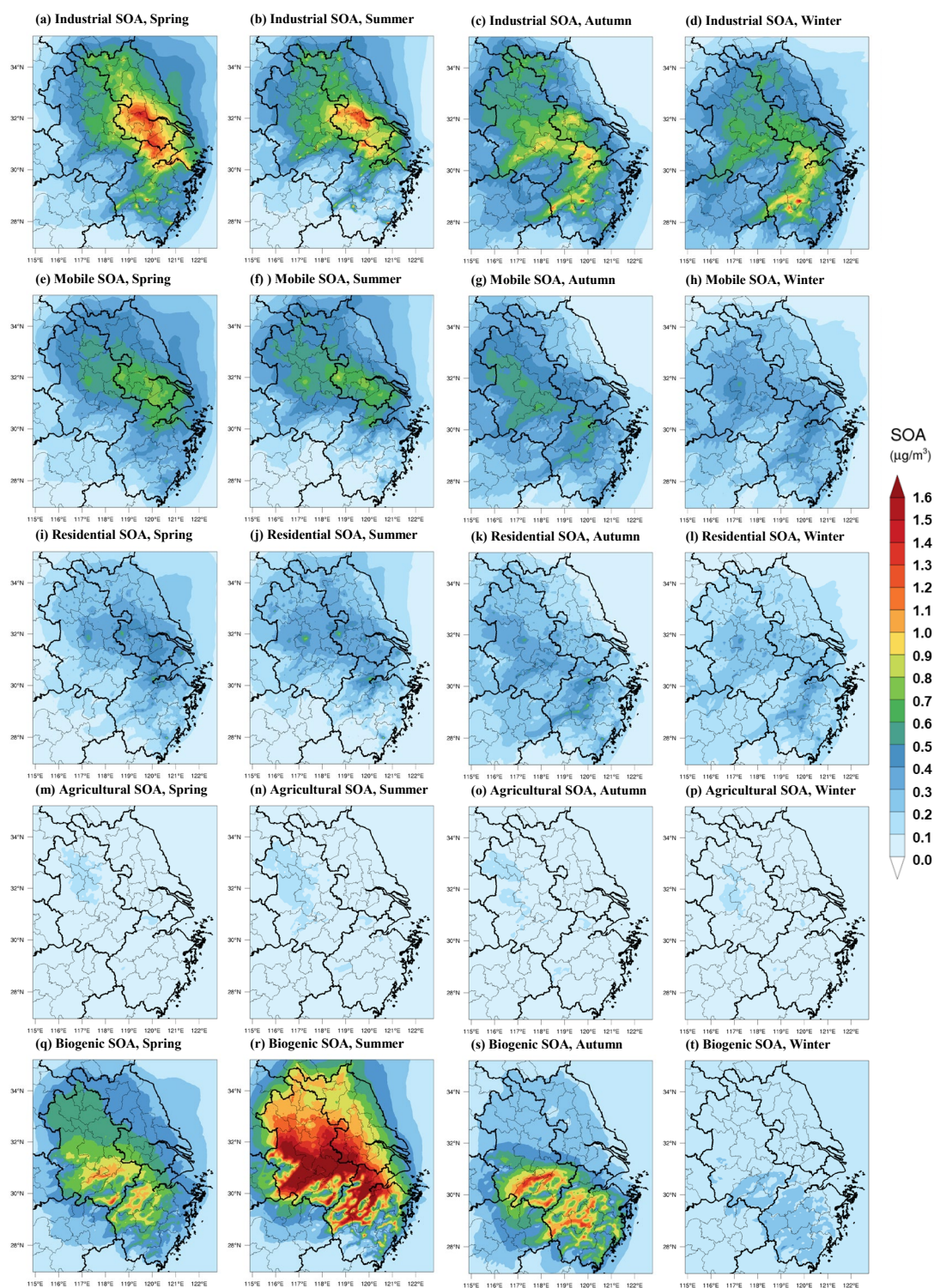
Figure 8. Spatial distributions of modeled SOA concentrations from different sources in each season in YRD region.

3.3.3 Predominant OA sources in sub-regions of YRD

To characterize the source contributions in different parts of the region, we

29

643 categorized the simulation region into six sub-regions: northern YRD, western YRD,

644 central YRD, eastern YRD and southern YRD. And six representative cities in theses

645 six regions were further selected for detailed comparison in source contributions,

646 including Xuzhou (XZ), Hefei (HF), Nanjing (NJ), Hangzhou (HZ), Shanghai (SH) and

647 Jinhua (JH). Figure 9 shows their locations and OA source contributions during summer
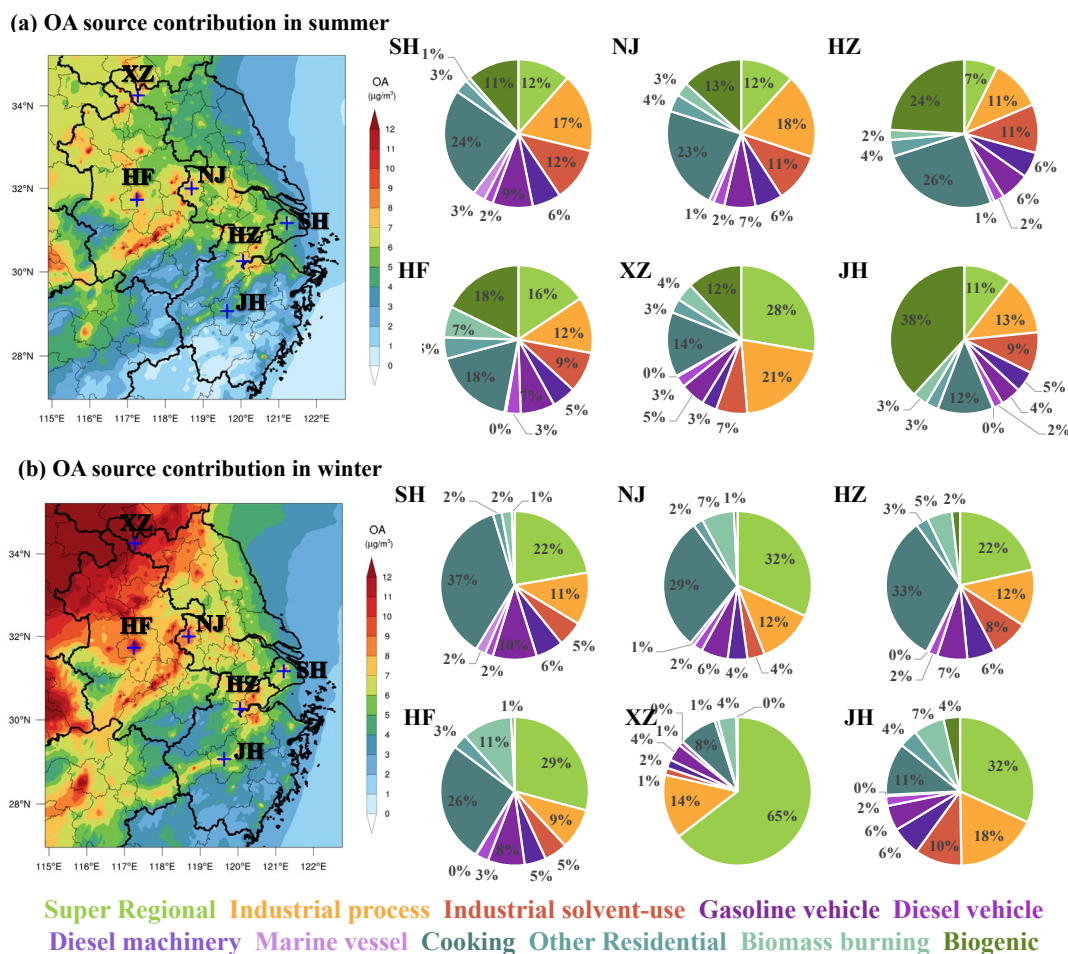
648 and winter.

649   In Northern YRD, represented by XZ, enhanced contribution from super-regional

650 scale to the local OA was observed for both winter (64.6%) and summer (27.7%) and

651 the contributions from industrial processes (14.0% in winter and 21.0% in summer)

652 were also higher than other sub-regions. Other major sources include biogenic (12.0%)

653 and cooking emissions (14.1%) in summer and cooking (8.3%) in winter. Taken

654 together, super-regional transportation and industrial processes are predominant

655 contributors of OA in northern YRD, accounting for 78.6% and 48.7% in summer and

656 winter respectively, followed by cooking emissions.

657   In western YRD, represented by HF, cooking emission was the largest contributor

658 to OA with contributions of 17.8% and 26.3% in both summer and winter respectively,

659 followed by super-regional contributions of 15.7% (summer) and 29.2% (winter). Other

660 major sources also include mobile source of 15.5%, biogenic source in summer (17.8%)

661 and industrial processes in both summer (12.3%) and winter (8.9%). In central YRD,

662 represented by NJ and HZ, the relative source contributions were very similar to those

663 in western YRD, with predominant contributions from cooking (22.8%-32.6%),

664 followed by super-regional transportation (7.4%-31.8%), industrial processes (11.3%-

665 18.4%) and mobile source (13.1%-16.3%).

666   In eastern YRD, represented by SH, the largest OA source was cooking emission,

667 account for 24.3% and 36.6% of OA in summer and winter respectively, followed by

668 mobile sources of 19%, super-regional transportation of 11.5% (summer) and 22.2%

669 (winter) and industrial processes of 17.3% (summer) and 11.4% (winter). In southern

670 YRD, represented by JH, while biogenic contribution was prevailing in summer

671   (38.2%), super-regional transportation was significant in winter (31.8%). Similar to

672   other sub-regions, other major sources also included the contributions of cooking

673   emission of 12.2% (summer) and 11.4% (winter), industrial processes of 12.9%

674   (summer) and 17.9% (winter) and mobile sources of 13%. Yet southern YRD presented

675   more evident increase in the contribution from industrial solvent-use compared with

676   other sub-regions.

677   To summarize, cooking, super-regional transportation, industrial process and mobile

678   sources were the predominant sources of OA in all sub-regions regardless of the season,

679   albeit enhanced contributions from biogenic sources to the OA formation in summer

680   was observed, especially in southern YRD. High contributions of cooking sources were

681   in accordance with the distributions of populations and high contributions of mobile

682   sources were somewhat expected, especially in the city centers. Source contributions of

683   OA varies in the intraregional scale implies that more targeted control measures need

684   to be designed according to the emission features of each city. Specifically, for densely

685   populated area, it is necessary to strengthen the future control strategy of cooking

686   emissions; special attention needs to be paid to the I/SVOC emissions from industrial

687   sources in eastern, central, and northern YRD region; mobile sources show its

688   significance in urban aera of the region, dominated by the equal contributions from

689   gasoline and diesel vehicles, indicating further reductions on the I/SVOCs from vehicle

690   emissions are therefore critical for pollution control on city scale.

(a) OA source contribution in summer

(b) OA source contribution in winter

Super Regional   Industrial process   Industrial solvent-use   Gasoline vehicle   Diesel vehicle
Diesel machinery   Marine vessel   Cooking   Other Residential   Biomass burning   Biogenic

Figure 9. Source contributions of modeled OA concentrations from different sources during summer and winter in different cities of the region.

4. Conclusions

In this study, we established a high-resolution I/SVOC emission inventory with detailed source profiles and applied it into CMAQ v5.3 to simulate POA and SOA formation in YRD region of China. With the addition of I/SVOC emissions, simulation results show significant improvements on both temporal variations and spatial distributions of OA. Compared with the BASE simulation, where I/SVOC emissions were not included, the simulated SOA increased by 1.5 times in IMPROVE simulation, highlighting the significant contributions of I/SVOC emissions to SOA production. The remaining 10%−30% underestimation of OA indicates that future work is still needed in bridging the gap between simulation and observations, such as, measuring local emission factors and source profiles of I/SVOC from various local sources, updating

705   SOA formation mechanisms in model framework.

706   With the addition of source specific I/SVOC emissions, we successfully quantified

707   the contribution of each source to POA and SOA concentrations in YRD. For POA,

708   cooking emission is the predominant source, which concentrates in urban area of YRD

709   in accordance with the population distribution. For SOA, for the first time, we

710   demonstrate that I/SVOCs from industrial sources are dominant contributor, followed

711   by those from mobile sources. In summer, the contributions of biogenic emission to

712   total SOA are also non-negligible, especially for the cities in southern YRD. Spatial and

713   seasonal variations in the source contributions suggest that control strategies for OA

714   pollution should vary by cities and seasons. On regional scale, cooking emissions has

715   been emerging as an important POA source, not to mention their impacts on SOA

716   formation are not yet certain. Our results suggest the control measures on the cooking

717   emissions should be strengthened in the future for the further reduction of POA. We

718   also found that SOA in the region is primarily contributed by industrial I/SVOC

719   emissions, which urges in-depth studies of emission factors and source profiles of

720   I/SVOC emissions from industrial sources as well as the corresponding control

721   measures. On intraregional scale, for urban area, continuous reduction in I/SVOC

722   emissions from mobile sources, especially gasoline and diesel vehicles, are effective

723   measures in the mitigation of urban air pollution, which is also technically feasible as

724   has been demonstrated in Qi et al. (2021). Continuous improvement in emission

725   standards is one way to promote the reduction of motor vehicle related SOA.

726   *Data availability*

727   The gridded emissions of I/SVOCs from various sources for the YRD region

728   developed by this study at a horizontal resolution of 4 km × 4 km can be downloaded

729   from the following website (https://doi.org/10.6084/m9.figshare.19536082.v1).

730   Additional related data are available upon request by contacting the corresponding

731   author (Cheng Huang; huangc@saes.sh.cn).

734 *Author contributions*

735   CH, JA, DH, and MQ designed the research. CH and JA developed the I/SVOC

736 emission inventory. JA, MQ, and RY performed the model. DH, LQ, MZ, YL, SZ, and

737 QW collected the observation data. CH, JA, DH, and HW analyzed the results. CH, JA,

738 and DH wrote the paper.

739 *Competing interests*

740   The authors declare that they have no conflict of interest.

752 **References**

753 An, J., Huang, Y., Huang, C., Wang, X., Yan, R., Wang, Q., Wang, H., Jing, S., Zhang, Y., Liu,

754   Y., Chen, Y., Xu, C., Qiao, L., Zhou, M., Zhu, S., Hu, Q., Lu, J., and Chen, C.: Emission

755   inventory of air pollutants and chemical speciation for specific anthropogenic sources

756   based on local measurements in the Yangtze River Delta region, China, Atmos. Chem.

757   Phys., 21, 2003–2025, 2021.

758 Boylan, J. W., and Russell, A. G.: PM and light extinction model performance metrics, goals,

759　　and criteria for three-dimensional air quality models, Atmos. Environ., 40, 4946–4959,

760　　2006.

761　Cai, S., Zhu, L., Wang, S., Wisthaler, A., Li, Q., Jiang, J., and Hao, J.: Time-resolved

762　　intermediate-volatility and semivolatile organic compound emissions from household coal

763　　combustion in northern China, Environ. Sci. Technol., 53, 9269−9278, 2019.

764　Canagaratna, M. R., Jayne, J. T., Jimenez, J. L., Allan, J. D., Alfarra, M. R., Zhang, Q., Onasch,

765　　T. B., Drewnick, F., Coe, H., Middlebrook, A., Delia, A., Williams, L. R., Trimborn, A. M.,

766　　Northway, M. J., DeCarlo, P. F., Kolb, C. E., Davidovits, P., and Worsnop, D. R.: Chemical

767　　and microphysical characterization of ambient aerosols with the aerodyne aerosol mass

768　　spectrometer, Mass Spectrom. Rev., 26, 185−222, 2007.

769　Canonaco, F., Crippa, M., Slowik, J. G., Baltensperger, U., and Prévôt, A. S. H.: SoFi, an IGOR-

770　　based interface for the efficient use of the generalized multilinear engine (ME-2) for the

771　　source apportionment: ME-2 application to aerosol mass spectrometer data, Atmos. Meas.

772　　Tech., 6, 3649–3661, 2013.

773　Chang, X., Zhao, B., Zheng, H., Wang, S., Cai, S., Guo, F., Gui, P., Huang, G., Wu, D., Han, L.,

774　　Xing, J., Man, H., Hu, R., Liang, C., Xu, Q., Qiu, X., Ding, D., Liu, K., Han, R., Robinson,

775　　A. L., and Donahue, N. M.: Full-volatility emission framework corrects missing and

776　　underestimated secondary organic aerosol sources, One Earth, 5, 403–412, 2022.

777　Chen, W., Ye, Y., Hu, W., Zhou, H., Pan, T., Wang, Y., Song, W., Song, Q., Ye, C., Wang, C.,

778　　Wang, B., Huang, S., Yuan, B., Zhu, M., Lian, X., Zhang, G., Bi, X., Jiang, F., Liu, J.,

779　　Canonaco, F., Prevot, A. S. H., Shao, M., and Wang, X.: Real-time characterization of

780　　aerosol compositions, sources, and aging processes in Guangzhou during PRIDE-GBA

781　　2018 campaign, J. Geophys. Res., Atmos., 126, e2021JD035114, 2021.

782　Crippa, M., Canonaco, F., Lanz, V. A., Äijälä, M., Allan, J. D., Carbone, S., Capes, G., Ceburnis,

783　　D., Dall'Osto, M., Day, D. A., DeCarlo, P. F., Ehn, M., Eriksson, A., Freney, E.,

784　　Hildebrandt Ruiz, L., Hillamo, R., Jimenez, J. L., Junninen, H., Kiendler-Scharr, A.,

785　　Kortelainen, A. M., Kulmala, M., Laaksonen, A., Mensah, A. A., Mohr, C., Nemitz, E.,

786　　O'Dowd, C., Ovadnevaite, J., Pandis, S. N., Petäjä, T., Poulain, L., Saarikoski, S., Sellegri,

K., Swietlicki, E., Tiitta, P., Worsnop, D. R., Baltensperger, U., and Prévôt, A. S. H.: Organic aerosol components derived from 25 AMS data sets across Europe using a consistent ME-2 based source apportionment approach, Atmos. Chem. Phys., 14, 6159–6176, 2014.

Cross, E. S., Hunter, J. F., Carrasquillo, A. J., Franklin, J. P., Herndon, S. C., Jayne, J. T., Worsnop, D. R., Miake-Lye, R. C., and Kroll, J. H.: Online measurements of the emissions of intermediate-volatility and semi-volatile organic compounds from aircraft, Atmos. Chem. Phys., 13, 7845–7858, 2013.

Decker, Z. C. J., Robinson, M. A., Barsanti, K. C., Bourgeois, I., Coggon, M. M., DiGangi, J. P., Diskin, G. S., Flocke, F. M., Franchin, A., Fredrickson, C. D., Gkatzelis, G. I., Hall, S. R., Halliday, H., Holmes, C. D., Gregory Huey, L., Lee, Y. R., Lindaas, J., Middlebrook, A. M., Montzka, D. D., Moore, R., Andrew Neuman, J., Nowak, J. B, Palm, B. B., Peischl, J., Piel, F., Rickly, P. S., Rollins, A. W., Ryerson, T. B., Schwantes, R. H., Sekimoto, K., Thornhill, L., Thornton, J. A., Tyndall, G. S., Ullmann, K., Van Rooy, P., Veres, P. R., Warneke, C., Washenfelder, R. A., Weinheimer, A. J., Wiggins, E., Winstead, E., Wisthaler, A., Womack, C., and Brown, S. S.: Nighttime and daytime dark oxidation chemistry in wildfire plumes: an observation and model analysis of FIREX-AQ aircraft data, Atmos. Chem. Phys., 21, 16293–16317, 2021.

Donahue, N. M., Robinson, A. L., and Pandis, S. N.: Atmospheric organic particulate matter: From smoke to secondary organic aerosol, Atmos. Environ., 43, 94–106, 2009.

Donahue, N. M., Robinson, A. L., Stanier, C. O., and Pandis, S. N.: Coupled Partitioning, Dilution, and Chemical Aging of Semivolatile Organics, Environ. Sci. Technol., 40, 2635–2643, 2006.

Drozd, G. T., Weber, R. J., and Goldstein, A. H.: Highly resolved composition during diesel evaporation with modeled ozone and secondary aerosol formation: Insights into pollutant formation from evaporative intermediate volatility organic compound sources, Environ. Sci. Technol., 55, 5742−5751, 2021.

Drozd, G. T., Zhao, Y., Saliba, G., Frodin, B., Maddox, C., Oliver Chang, M.-C., Maldonado,

815   H., Sardar, S., Weber, R. J., Robinson, A. L., and Goldstein, A. H.: Detailed speciation of

816   intermediate volatility and semivolatile organic compound emissions from gasoline

817   vehicles: Effects of cold-starts and implications for secondary organic aerosol formation,

818   Environ. Sci. Technol., 53, 1706–1714, 2019.

819 Emery, C., Tai, E., and Yarwood, G.: Enhanced meteorological modeling and performance

820   evaluation for two Texas ozone episodes, Prepared for the Texas natural resource

821   conservation commission, by ENVIRON International Corporation, 2001.

822 Gentner, D. R., Isaacman, G., Worton, D. R., Chan, A. W. H., Dallmann, T. R., Davis, L., Liu,

823   S., Day, D. A., Russell, L. M., Wilson, K. R., Weber, R., Guha, A., Harley, R. A., and

824   Goldstein, A. H.: Elucidating secondary organic aerosol from diesel and gasoline vehicles

825   through detailed characterization of organic carbon emissions, Proc. Natl. Acad. Sci., 109,

826   18318−18323, 2012.

827 Guo, J., Zhou, S., Cai, M., Zhao, J., Song, W., Zhao, W., Hu, W., Sun, Y., He, Y., Yang, C., Xu,

828   X., Zhang, Z., Cheng, P., Fan, Q., Hang, J., Fan, S., Wang, X., and Wang, X.:

829   Characterization of submicron particles by time-of-flight aerosol chemical speciation

830   monitor (ToF-ACSM) during wintertime: aerosol composition, sources, and chemical

831   processes in Guangzhou, China, Atmos. Chem. Phys., 20, 7595–7615, 2020.

832 Hallquist, M., Wenger, J. C., Baltensperger, U., Rudich, Y., Simpson, D., Claeys, M., Dommen,

833   J., Donahue, N. M., George, C., Goldstein, A. H., Hamilton, J. F., Herrmann, H., Hoffmann,

834   T., Iinuma, Y., Jang, M., Jenkin, M. E., Jimenez, J. L., Kiendler-Scharr, A., Maenhaut, W.,

835   McFiggans, G., Mentel, Th. F., Monod, A., Prévôt, A. S. H., Seinfeld, J. H., Surratt, J. D.,

836   Szmigielski, R., and Wildt, J.: The formation, properties and impact of secondary organic

837   aerosol: Current and emerging issues, Atmos. Chem. Phys., 9, 5155–5236, 2009.

838 Hayes, P. L., Ortega, A. M., Cubison, M. J., Froyd, K. D., Zhao, Y., Cliff, S. S., Hu, W. W.,

839   Toohey, D. W., Flynn, J. H., Lefer, B. L., Grossberg, N., Alvarez, S., Rappenglück, B.,

840   Taylor, J. W., Allan, J. D., Holloway, J. S., Gilman, J. B., Kuster, W. C., de Gouw, J. A.,

841   Massoli, P., Zhang, X., Liu, J., Weber, R. J., Corrigan, A. L., Russell, L. M., Isaacman, G.,

842   Worton, D. R., Kreisberg, N. M., Goldstein, A. H., Thalman, R., Waxman, E. M., Volkamer,

843   R., Lin, Y. H., Surratt, J. D., Kleindienst, T. E., Offenberg, J. H., Dusanter, S., Griffith, S.,

844   Stevens, P. S., Brioude, J., Angevine, W. M., and Jimenez, J. L.: Organic aerosol

845   composition and sources in Pasadena, California, during the 2010 CalNex campaign, J.

846   Geophys. Res., Atmos., 118, 9233–9257, 2013.

847 Huang, C., Hu, Q., Li, Y., Tian, J., Ma, Y., Zhao, Y., Feng, J., An, J., Qiao, L., Wang, H., Jing,

848   S., Huang, D., Lou, S., Zhou, M., Zhu, S., Tao, S., and Li, L.: Intermediate volatility

849   organic compound emissions from a large cargo vessel operated under real-world

850   conditions, Environ. Sci. Technol., 52, 12934–12942, 2018.

851 Huang, D., Zhu, S., An, J., Wang, Q., Qiao, L., Zhou, M., He, X., Ma, Y., Sun, Y., Huang, C.,

852   Yu, J., and Zhang, Q.: Comparative assessment of cooking emission contributions to urban

853   organic aerosol using online molecular tracers and aerosol mass spectrometry

854   measurements, Environ. Sci. Technol., 55, 14526–14535, 2021.

855 Huang, L., Wang, Q., Wang, Y., Emery, C., Zhu, A., Zhu, Y., Yin, S., Yarwood, G., Zhang, K.,

856   and Li, L.: Simulation of secondary organic aerosol over the Yangtze River Delta region:

857   The impacts from the emissions of intermediate volatility organic compounds and the SOA

858   modeling framework, Atmos. Environ., 246, 118079, 2021b.

859 Huang, R. J., Zhang, Y., Bozzetti, C., Ho, K., Cao, J., Han, Y., Daellenbach, K. R., Slowik, J.

860   G., Platt, S. M., Canonaco, F., Zotter, P., Wolf, R., Pieber, S. M., Bruns, E. A., Crippa, M.,

861   Ciarelli, G., Piazzalunga, A., Schwikowski, M., Abbaszade, G., Schnelle-Kreis, J.,

862   Zimmermann, R., An, Z., Szidat, S., Baltensperger, U., El Haddad, I., and Prévôt, A. S. H.:

863   High secondary aerosol contribution to particulate pollution during haze events in China,

864   Nature, 514, 218–222, 2014.

865 Huffman, J., Docherty, K., Mohr, C., Cubison, M., Ulbrich, I., Ziemann, P., Onasch, T., and

866   Jimenez, J.: Chemically-resolved volatility measurements of organic aerosol from

867   different sources, Environ. Sci. Technol., 43, 5351–5357, 2009.

868 Jathar, S. H., Gordon, T. D., Hennigan, C. J., Pye, H. O. T., Pouliot, G., Adams, P. J., Donahue,

869   N. M., and Robinson, A. L.: Unspeciated organic emissions from combustion sources and

870   their influence on the secondary organic aerosol budget in the United States, P. Natl. Acad.

871   Sci. USA, 111, 10473–10478, 2014.

872 Jathar, S. H., Woody, M., Pye, H. O. T., Baker, K. R., and Robinson, A. L.: Chemical transport

873   model simulations of organic aerosol in southern California: model evaluation and

874   gasoline and diesel source contributions, Atmos. Chem. Phys., 17, 4305–4318, 2017.

875 Jimenez, J. L., Canagaratna, M. R., Donahue, N. M., Prevot, A. S. H., Zhang, Q., Kroll, J. H.,

876   DeCarlo, P. F., Allan, J. D., Coe, H., Ng, N. L., Aiken, A. C., Docherty, K. S., Ulbrich, I.

877   M., Grieshop, A. P., Robinson, A. L., Duplissy, J., Smith, J. D., Wilson, K. R., Lanz, V. A.,

878   Hueglin, C., Sun, Y. L., Tian, J., Laaksonen, A., Raatikainen, T., Rautiainen, J., Vaattovaara,

879   P., Ehn, M., Kulmala, M., Tomlinson, J. M., Collins, D. R., Cubison, M. J., Dunlea, J.,

880   Huffman, J. A., Onasch, T. B., Alfarra, M. R., Williams, P. I., Bower, K., Kondo, Y.,

881   Schneider, J., Drewnick, F., Borrmann, S., Weimer, S., Demerjian, K., Salcedo, D., Cottrell,

882   L., Griffin, R., Takami, A., Miyoshi, T., Hatakeyama, S., Shimono, A., Sun, J. Y., Zhang,

883   Y. M., Dzepina, K., Kimmel, J. R., Sueper, D., Jayne, J. T., Herndon, S. C., Trimborn, A.

884   M., Williams, L. R., Wood, E. C., Middlebrook, A. M., Kolb, C. E., Baltensperger, U., and

885   Worsnop, D. R.: Evolution of Organic Aerosols in the Atmosphere, Science, 326, 1525–

886   1529, 2009.

887 Kim, D., Cho, C., Jeong, S., Lee, S., Nault, B. A., Campuzano-Jost, P., Day, D. A., Schroder, J.

888   C., Jimenez, J. L., Volkamer, R., Blake, D. R., Wisthaler, A., Fried, A., DiGangi, J. P.,

889   Diskin, G. S., Pusede, S. E., Hall, S. R., Ullmann, K., Gregory Huey, L., Tanner, D. J.,

890   Dibb, J., Knote, C. J., and Min, K., Field observational constraints on the controllers in

891   glyoxal (CHOCHO) reactive uptake to aerosol, Atmos. Chem. Phys., 22, 805–821, 2022.

892 Kim, Y., Couvidat, F., Sartelet, K., and Seigneur, C.: Comparison of different gas-phase

893   mechanisms and aerosol modules for simulating particulate matter formation, J. Air Waste

894   Manage., 61, 1218–1226, 2011.

895 Koo, B., Knipping, E., and Yarwood, G.: 1.5-Dimensional volatility basis set approach for

896   modeling organic aerosol in CAMx and CMAQ, Atmos. Environ., 95, 158–164, 2014.

897 Koss, A. R., Sekimoto, K., Gilman, J. B., Selimovic, V., Coggon, M. M., Zarzana, K. J., Yuan,

898   B., Lerner, B. M., Brown, S. S., Jimenez, J. L., Krechmer, J., Roberts, J. M., Warneke, C.,

899 Yokelson, R. J., and de Gouw, J.: Non-methane organic gas emissions from biomass

900 burning: identification, quantification, and emission factors from PTR-ToF during the

901 FIREX 2016 laboratory experiment, Atmos. Chem. Phys., 18, 3299–3319, 2018.

902 Li, J., Cao, L., Gao, W., He, L., Yan, Y., He, Y., Pan, Y., Ji, D., Liu, Z., and Wang, Y.: Seasonal

903 variations in the highly time-resolved aerosol composition, sources and chemical

904 processes of background submicron particles in the North China Plain, Atmos. Chem.

905 Phys., 21, 4521–4539, 2021.

906 Li, J., Han, Z., Li, J., Liu, R., Wu, Y., Liang, L., and Zhang, R.: The formation and evolution of

907 secondary organic aerosol during haze events in Beijing in wintertime, Sci. Total Environ.,

908 703, 134937, 2020.

909 Li, J., Han, Z., Wu, J., Tao, J., Li, J., Sun, Y., Liang, L., Liang, M., and Wang, Q.: Secondary

910 organic aerosol formation and source contributions over east China in summertime,

911 Environ. Pollut., 306, 119383, 2022.

912 Li, M., Zhang, Q., Kurokawa, J. i., Woo, J. H., He, K., Lu, Z., Ohara, T., Song, Y., Streets, D.

913 G., Carmichael, G. R., Cheng, Y., Hong, C., Huo, H., Jiang, X., Kang, S., Liu, F., Su, H.,

914 Zheng, B.: MIX: a mosaic Asian anthropogenic emission inventory under the international

915 collaboration framework of the MICS-Asia and HTAP. Atmos. Chem. Phys., 17, 935–963,

916 2017.

917 Li, Y., Ren, B., Qiao, Z., Zhu, J., Wang, H., Zhou, M., Qiao, L., Lou, S., Jing, S., Huang, C.,

918 Tao, S., Rao, P., and Li, J.: Characteristics of atmospheric intermediate volatility organic

919 compounds (IVOCs) in winter and summer under different air pollution levels, Atmos.

920 Environ., 210, 58–65, 2019.

921 Li, Y. J., Sun, Y. L., Zhang, Q., Li, X., Li, M., Zhou, Z., and Chan, C. K.: Real-time chemical

922 characterization of atmospheric particulate matter in China: A review, Atmos. Environ.,

923 158, 270–304, 2017.

924 Liggio, J., Li, S., Hayden, K., Taha, Y. M., Stroud, C., Darlington, A., Drollette, B. D., Gordon,

925 M., Lee, P., Liu, P., Leithead, A., Moussa, S. G., Wang, D., Brien, J. O., Mittermeier, R.

926 L., Osthoff, H. D., Makar, P. A., Zhang, J., Brook, J. R., Lu, G., Staebler, R. M., Han, Y.,

927   Travis, W., Plata, D. L., and Gentner, D. R.: Oil sands operations as a large source of

928   secondary organic aerosols, Nature, 534, 1–16, 2016.

929   Ling, Z., Wu, L., Wang, Y., Shao, M., Wang, X., and Huang, W.: Roles of semivolatile and

930   intermediate-volatility organic compounds in secondary organic aerosol formation and its

931   implication: A review, J. Environ. Sci., 114, 259–285, 2022.

932   Liu, H., Man, H., Cui, H., Wang, Y., Deng, F., Wang, Y., Yang, X., Xiao, Q., Zhang, Q., Ding,

933   Y., and He, K.: An updated emission inventory of vehicular VOCs and IVOCs in China,

934   Atmos. Chem. Phys., 17, 12709–12724, 2017.

935   Liu, H., Meng, Z., Lv, Z., Wang, X., Deng, F., Liu, Y., Zhang, Y., Shi, M., Zhang, Q., and He,

936   K.: Emissions and health impacts from global shipping embodied in US–China bilateral

937   trade, Nat. Sustain., 2, 1027–1033, 2019.

938   Liu, Y., Li, L., An, J., Huang, L., Yan, R., Huang, C., Wang, H., Wang, Q., Wang, M., and Zhang,

939   W.: Estimation of biogenic VOC emissions and its impact on ozone formation over the

940   Yangtze River Delta region, China, Atmos. Environ., 186, 113–128, 2018a.

941   Liu, Z., Gao, W., Yu, Y., Hu, B., Xin, J., Sun, Y., Wang, L., Wang, G., Bi, X., Zhang, G., Xu, H.,

942   Cong, Z., He, J., Xu, J., and Wang, Y.: Characteristics of PM2.5 mass concentrations and

943   chemical species in urban and background areas of China: emerging results from the

944   CARE-China network, Atmos. Chem. Phys., 18, 8849–8871, 2018b.

945   Louvaris, E. E., Florou, K., Karnezi, E., Papanastasiou, D. K., Gkatzelis, G. I., and Pandis, S.

946   N.: Volatility of source apportioned wintertime organic aerosol in the city of Athens,

947   Atmos. Environ., 158, 138–147, 2017.

948   Lu, Q., Murphy, B. N., Qin, M., Adams, P. J., Zhao, Y., Pye, H. O. T., Efstathiou, C., Allen, C.,

949   and Robinson, A. L.: Simulation of organic aerosol formation during the CalNex study:

950   Updated mobile emissions and secondary organic aerosol parameterization for

951   intermediate-volatility organic compounds, Atmos. Chem. Phys., 20, 4313–4332, 2020.

952   Lu, Q., Zhao, Y., and Robinson, A. L.: Comprehensive organic emission profiles for gasoline,

953   diesel, and gas-turbine engines including intermediate and semi-volatile organic

954   compound emissions, Atmos. Chem. Phys., 18, 17637–17654, 2018.

955   May, A. A., Levin, E. J. T., Hennigan, C. J., Riipinen, I., Lee, T., Collett, J. L., Jimenez, J. L.,

956   Kreidenweis, S. M., and Robinson, A. L.: Gas-particle partitioning of primary organic

957   aerosol emissions: 3. Biomass burning, J. Geophys. Res.-Atmos., 118, 11327–11338, 2013.

958   McDonald, B. C., de Gouw, J. A., Gilman, J. B., Jathar, S. H., Akherati, A., Cappa, C. D.,

959   Jimenez, J. L., Lee-Taylor, J., Hayes, P. L., McKeen, S. A., Cui, Y. Y., Kim, S., Gentner,

960   D. R., Isaacman-VanWertz, G., Goldstein, A. H., Harley, R. A., Frost, G. J., Roberts, J. M.,

961   Ryerson, T. B., and Trainer, M.: Volatile chemical products emerging as largest

962   petrochemical source of urban organic emissions, Science, 359, 760–764, 2018.

963   Miao, R., Chen, Q., Shrivastava, M., Chen, Y., Zhang, L., Hu, J., Zheng, Y., and Liao, K.:

964   Process-based and observation-constrained SOA simulations in China: the role of

965   semivolatile and intermediate-volatility organic compounds and OH levels, Atmos. Chem.

966   Phys., 21, 16183–16201, 2021.

967   Ming, L., Jin, L., Li, J., Fu, P., Yang, W., Liu, D., Zhang, G., Wang, Z., and Li, X.: $PM_{2.5}$ in the

968   Yangtze River Delta, China: Chemical compositions, seasonal variations, and regional

969   pollution events, Environ. Pollut., 223, 200–212, 2017.

970   Murphy, B. N., Woody, M. C., Jimenez, J. L., Carlton, A. M. G., Hayes, P. L., Liu, S., Ng, N.

971   L., Russell, L. M., Setyan, A., and Xu, L.: Semivolatile POA and parameterized total

972   combustion SOA in CMAQv5.2: impacts on source strength and partitioning, Atmos.

973   Chem. Phys., 17, 11107–11133, 2017.

974   Nault, B. A., Jo, D. S., McDonald, B. C., Campuzano-Jost, P., Day, D. A., Hu, W., Schroder, J.

975   C., Allan, J., Blake, D. R., Canagaratna, M. R., Coe, H., Coggon, M. M., DeCarlo, P. F.,

976   Diskin, G. S., Dunmore, R., Flocke, F., Fried, A., Gilman, J. B., Gkatzelis, G., Hamilton,

977   J. F., Hanisco, T. F., Hayes, P. L., Henze, D. K., Hodzic, A., Hopkins, J., Hu, M., Huey, L.

978   G., Jobson, B. T., Kuster, W. C., Lewis, A., Li, M., Liao, J., Nawaz, M. O., Pollack, I. B.,

979   Peischl, J., Rappenglück, B., Reeves, C. E., Richter, D., Roberts, J. M., Ryerson, T. B.,

980   Shao, M., Sommers, J. M., Walega, J., Warneke, C., Weibring, P., Wolfe, G. M., Young, D.

981   E., Yuan, B., Zhang, Q., de Gouw, J. A., and Jimenez, J. L.: Secondary organic aerosols

982   from anthropogenic volatile organic compounds contribute substantially to air pollution

983   mortality, Atmos. Chem. Phys., 21, 11201–11224, 2021.

984   Presto, A. A., Miracolo, M. A., Kroll, J. H., Worsnop, D. R., Robinson, A. L., and Donahue, N.

985   M.: Intermediate-volatility organic compounds: A potential source of ambient oxidized

986   organic aerosol, Environ. Sci. Technol., 43, 4744–4749, 2009.

987   Presto, A. A., Nguyen, N. T., Ranjan, M., Reeder, A. J., Lipsky, E. M., Hennigan, C. J., Miracolo,

988   M. A., Riemer, D. D., and Robinson, A. L.: Fine particle and organic vapor emissions from

989   staged tests of an in-use aircraft engine, Atmos. Environ., 45, 3603–3612, 2011.

990   Pye, H. O. T., Seinfeld, J. H.: A global perspective on aerosol from low-volatility organic

991   compounds, Atmos. Chem. Phys., 10, 4377–4401, 2010.

992   Qi, L., Liu, H., Shen, X., Fu, M., Huang, F., Man, H., Deng, F., Shaikh, A. A., Wang, X., Dong,

993   R., Song, C., and He, K.: Intermediate-volatility organic compound emissions from

994   nonroad construction machinery under different operation modes, Environ. Sci. Technol.,

995   53, 13832–13840, 2019.

996   Qi, L., Zhao, J., Li, Q., Su, S., Lai, Y., Deng, F., Man, H., Wang, X., Shen, X., Lin, Y., Ding, Y.,

997   and Liu, H.: Primary organic gas emissions from gasoline vehicles in China: Factors,

998   composition and trends, Environ. Pollut., 290, 117984, 2021.

999   Qin, M., Hu, A., Mao, J., Li, X., Sheng, L., Sun, J., Li, J., Wang, X., Zhang, Y., Hu, J.: $PM_{2.5}$

1000   and O_3 relationships affected by the atmospheric oxidizing capacity in the Yangtze River

1001   Delta, China, Sci. Total Environ., 810, 152268, 2022.

1002   Ren, B., Zhu, J., Tian, L., Wang, H., Huang, C., Jing, S., Lou, S., An, J., Lu, J., Rao, P., Fu, Q.,

1003   Huo, J., and Li, Y.: An alternative semi-quantitative GC/MS method to estimate levels of

1004   airborne intermediate volatile organic compounds (IVOCs) in ambient air, Atmos.

1005   Environ., X6, 100075, 2020.

1006   Robinson, A. L., Donahue, N. M., Shrivastava, M. K., Weitkamp, E. A., Sage, A. M., Grieshop,

1007   A. P., Lane, T. E., Pierce, J. R., and Pandis, S. N.: Rethinking organic aerosols:

1008   Semivolatile emissions and photochemical aging, Science, 315, 1259–1262, 2007.

1009   Sartelet, K., Zhu, S., Moukhtar, S., André, M., Gros, V., Favez, O., Brasseurh, A., and Redaelli,

1010   M.: Emission of intermediate, semi and low volatile organic compounds from traffic and

their impact on secondary organic aerosol concentrations over greater paris, Atmos. Environ, 180, 126–137, 2018.

Shrivastava, M. K., Cappa, C. D., Fan, J., Goldstein, A. H., Guenther, A. B., Jimenez, J. L., Kuang, C., Laskin, A., Martin, S. T., Ng, N. L., Petaja, T., Pierce, J. R., Rasch, P. J., Roldin, P., Seinfeld, J. H., Shilling, J., Smith, J. N., Thornton, J. A., Volkamer, R., Wang, J., Worsnop, D. R., Zaveri, R. A., Zelenyuk, A., and Zhang, Q.: Recent advances in understanding secondary organic aerosol: Implications for global climate forcing, Rev. Geophys., 55, 509–559, 2017.

Shrivastava, M., Fast, J., Easter, R., Gustafson, W. I., Zaveri, R. A., Jimenez, J. L., Saide, P., and Hodzic, A.: Modeling organic aerosols in a megacity: comparison of simple and complex representations of the volatility basis set approach, Atmos. Chem. Phys., 11, 6639–6662, 2011.

Sun, Y., Jiang, Q., Wang, Z., Fu, P., Li, J., Yang, T., and Yin, Y.: Investigation of the sources and evolution processes of severe haze pollution in Beijing in January 2013, J. Geophys. Res., Atmos., 119, 4380–4398, 2014.

Tang, J., Li, Y., Li, X., Jing, S., Huang, C., Zhu, J., Hu, Q., Wang, H., Lu, J., Lou, S., Rao, P., and Huang, D.: Intermediate volatile organic compounds emissions from vehicles under real world conditions, Sci. Total Environ., 788, 147795, 2021.

Tao, J., Zhang, L., Cao, J., and Zhang, R.: A review of current knowledge concerning $PM_{2.5}$ chemical composition, aerosol optical properties and their relationships across China, Atmos. Chem. Phys., 17, 9485–9518, 2017.

Tkacik, D. S., Presto, A. A., Donahue, N. M., and Robinson, A. L.: Secondary organic aerosol formation from intermediate-volatility organic compounds: Cyclic, linear, and branched alkanes, Environ. Sci. Technol., 46, 8773–8781, 2012.

Tsimpidi, A. P., Karydis, V. A., Zavala, M., Lei, W., Molina, L., Ulbrich, I. M., Jimenez, J. L., and Pandis, S. N.: Evaluation of the volatility basis-set approach for the simulation of organic aerosol formation in the Mexico City metropolitan area, Atmos. Chem. Phys., 10, 525–546, 2010.

US EPA: Final Report, SPECIATE Version 5.1, Database Development Documentation, available at: https://www.epa.gov/air-emissions-modeling/speciate-51-and-50-addendum-and-final-report (last access: 8 August 2021), 2021

Woody, M. C., Baker, K. R., Hayes, P. L., Jimenez, J. L., Koo, B., and Pye, H. O. T.: Understanding sources of organic aerosol during CalNex-2010 using the CMAQ-VBS, Atmos. Chem. Phys., 16, 4081–4100, 2016.

Wu, L., Ling, Z., Liu, H., Shao, M., Lu, S., Wu, L., and Wang, X.: A gridded emission inventory of semi-volatile and intermediate volatility organic compounds in China, Sci. Total Environ., 761, 143295, 2021.

Wu, L., Wang, X., Lu, S., Shao, M., and Ling, Z.: Emission inventory of semi-volatile and intermediate-volatility organic compounds and their effects on secondary organic aerosol over the Pearl River Delta region, Atmos. Chem. Phys., 19, 8141–8161, 2019.

Xu, L., Guo, H., Boyd, C. M., Klein, M., Bougiatioti, A., Cerully, K. M., Hite, J. R., Isaacman-VanWertze, G., Kreisberg, N. M., Knote, C., Olson, K., Koss, A., Goldstein, A. H., Hering, S. V., de Gouw, J., Baumann, K., Lee, S., Nenes, A., Weber, R. J., and Ng, N. L.: Effects of anthropogenic emissions on aerosol formation from isoprene and monoterpenes in the southeastern United States, P. Natl. Acad. Sci. USA, 112, 37–42, 2015.

Yang, W., Li, J., Wang, W., Li, J., Ge, M., Sun, Y., Chen, X., Ge, B., Tong, S., Wang, Q., and Wang, Z.: Investigating secondary organic aerosol formation pathways in China during 2014, Atmos. Environ., 213, 133–147, 2019.

Yao, T., Li, Y., Gao, J., Fung, J. C. H., Wang, S., Li, Y., Chan, C. K., and Lau, A. K. H.: Source apportionment of secondary organic aerosols in the Pearl River Delta region: Contribution from the oxidation of semi-volatile and intermediate volatility primary organic aerosols, Atmos. Environ., 222, 117111, 2020.

Yu, K., Zhu, Q., Du, K., and Huang, X.: Characterization of nighttime formation of particulate organic nitrates based on high-resolution aerosol mass spectrometry in an urban atmosphere in China, Atmos. Chem. Phys., 19, 5235–5249, 2019.

Yuan, B., Shao, M., Lu, S., and Wang, B.: Source profiles of volatile organic compounds

1067   associated with solvent use in Beijing, China, Atmos. Environ., 44, 1919–1926, 2010.

1068 Zhang, H, Yee, L. D., Lee, B. H., Curtis, M. P., Worton, D. R., Isaacman-VanWertz, G.,

1069   Offenberg, J. H., Lewandowski, M., Kleindienst, T. E., Beaver, M. R., Holder, A. L.,

1070   Lonneman, W. A., Docherty, K. S., Jaoui, M., Pye, H. T. O., Hu, W., Day, D. A.,

1071   Campuzano-Jost, P., Jimenez, J. L., Guo, H., Weber, R. J., de Gouw, J., Koss, A. R.,

1072   Edgerton, E. S., Brune, W., Mohr, C., Lopez-Hilfiker, F. D., Lutz, A., Kreisberg, N. M.,

1073   Spielman, S. R., Hering, S. V., Wilson, K. R., Thornton, J. A., and Goldstein, A. H.:

1074   Monoterpenes are the largest source of summertime organic aerosol in the southeastern

1075   United States, P. Natl. Acad. Sci. USA, 115, 2038–2043, 2018.

1076 Zhang, Q., Jimenez, J. L., Canagaratna, M. R., Allan, J. D., Coe, H., Ulbrich, I., Alfarra, M. R.,

1077   Takami, A., Middlebrook, A. M., Sun, Y. L., Dzepina, K., Dunlea, E., Docherty, K.,

1078   DeCarlo, P. F., Salcedo, D., Onasch, T., Jayne, J. T., Miyoshi, T., Shimono, A., Hatakeyama,

1079   S., Takegawa, N., Kondo, Y., Schneider, J., Drewnick, F., Borrmann, S., Weimer, S.,

1080   Demerjian, K., Williams, P., Bower, K., Bahreini, R., Cottrell, L., Griffin, R. J., Rautiainen,

1081   J., Sun, J. Y., Zhang, Y. M., and Worsnop, D. R.: Ubiquity and dominance of oxygenated

1082   species in organic aerosols in anthropogenically-influenced Northern Hemisphere

1083   midlatitudes, Geophys. Res. Lett., 34, L13801, 2007.

1084 Zhang, Q., Jimenez, J. L., Canagaratna, M. R., Ulbrich, I. M., Ng, N. L., Worsnop, D. R., and

1085   Sun, Y.: Understanding atmospheric organic aerosols via factor analysis of aerosol mass

1086   spectrometry: a review, Anal. Bioanal. Chem., 401, 3045−3067, 2011.

1087 Zhang, Y., Vijayaraghavan, K., and Seigneur, C.: Evaluation of three probing techniques in a

1088   three-dimensional air quality model, J. Geophys. Res., Atmos., 110, D02305, 2005.

1089 Zhao, B., Wang, S., Donahue, N. M., Jathar, S. H., Huang, X. F., Wu, W., Hao, J., and Robinson,

1090   A. L.: Quantifying the effect of organic aerosol aging and intermediate-volatility emissions

1091   on regional scale aerosol pollution in China, Sci. Rep., 6, 28815, 2016a.

1092 Zhao, Y., Hennigan, C. J., May, A. A., Tkacik, D. S., De Gouw, J. A., Gilman, J. B., Kuster, W.

1093   C., Borbon, A., and Robinson, A. L.: Intermediate-volatility organic compounds: A large

1094   source of secondary organic aerosol, Environ. Sci. Technol., 48, 13743–13750, 2014.

1095   Zhao, Y., Kreisberg, N. M., Worton, D. R., Isaacman, G., Weber, R. J., Liu, S., Day, D. A.,

1096   Russell, L. M., Markovic, M. Z., VandenBoer, T. C., Murphy, J. G., Hering, S. V., and

1097   Goldstein, A. H.: Insights into secondary organic aerosol formation mechanisms from

1098   measured gas/particle partitioning of specific organic tracer compounds, Environ. Sci.

1099   Technol., 47, 3781−3787, 2013.

1100   Zhao, Y., Nguyen, N. T., Presto, A. A., Hennigan, C. J., May, A. A., and Robinson, A. L.:

1101   Intermediate volatility organic compound emissions from on-road diesel vehicles:

1102   Chemical composition, emission Factors, and estimated secondary organic aerosol

1103   production, Environ. Sci. Technol., 49, 11516–11526, 2015.

1104   Zhao, Y., Nguyen, N. T., Presto, A. A., Hennigan, C. J., May, A. A., and Robinson, A. L.:

1105   Intermediate Volatility Organic Compound Emissions from On-Road Gasoline Vehicles

1106   and Small Off-Road Gasoline Engines, Environ. Sci. Technol., 50, 4554–4563, 2016b.

1107   Zheng, M., Cass, G. R., Schauer, J. J., and Edgerton, E. S.: Source Apportionment of $PM_{2.5}$ in

1108   the Southeastern United States Using Solvent-Extractable Organic Compounds as Tracers,

1109   Environ. Sci. Technol., 36, 2361−2371, 2002.

1110   Zhu, S., Wang, Q., Qiao, L., Zhou, M., Wang, S., Lou, S., Huang, D., Wang, Q., Jing, S., Wang,

1111   H., Chen, C., Huang, C., and Yu, J. Z.: Tracer-based characterization of source variations

1112   of $PM_{2.5}$ and organic carbon in Shanghai influenced by the COVID-19 lockdown, Faraday

1113   Discuss., 226, 112, 2021.

1114   Zhu, W., Zhou, M., Cheng, Z., Yan, N., Huang, C., Qiao, L., Wang, H., Liu, Y., Lou, S., and

1115   Guo, S.: Seasonal variation of aerosol compositions in Shanghai, China: Insights from

1116   particle aerosol mass spectrometer observations, Sci. Total Environ., 771, 144948, 2021.

1117